FIBER BASED NON-LINEAR EXCITATION FLUORESCENCE MICROSCOPY

by

PRIYANKA AMRITA JILLELLA

Presented to the Faculty of the Graduate School of

The University of Texas at Arlington and

The University of Texas Southwestern Medical Center in Dallas

in Partial Fulfillment of the Requirements

for the Degree of

MASTER OF SCIENCE IN BIOMEDICAL ENGINEERING

THE UNIVERSITY OF TEXAS AT ARLINGTON

May 2007

And God said, "Let there be light" and there was light.

ACKNOWLEDGEMENTS

This thesis is a result one and a half years of work, cunctation, learning, patience and encouragement. And, I acknowledge myself for the first three in the list which variably have aided and impeded the completion of this thesis. The next two in the list have been the most significant external factors that unarguably catalyzed the successful completion of the thesis, for which I cannot be enough grateful.

Dr. Dave, I am grateful for giving me the opportunity to work on such interesting projects. You introduced me to the field optics and helped me in understanding optics better, for which I will always be indebted in gratitude to you. I am also thankful for your patience with me throughout the course of this work. Thank you!

Dr. Jamboor Vishwanatha, Dr. Kytai Nguyen and Dr. George Alexandrakis, my sincere thanks to you for serving on my thesis committee.

Thank you Daddy, for your love and support throughout my life. You are the bestest. Thank you Mummy, for your love and prayers without which nothing of this would be possible. Thank you to my sister, who loves me much and whom I love much.

My special gratitude to my friends and lab mates for their sound and timely advice, good company and most importantly encouragement. I am grateful.

December 5, 2006

ABSTRACT

FIBER BASED NON-LINEAR EXCITATION FLUORESCENCE MICROSCOPY

Publication No. _____

PRIYANKA AMRITA JILLELLA, M.S.

The University of Texas at Arlington, 2007

Supervising Professor: Dr. Digant Dave

Non-linear excitation fluorescence microscopy is a high resolution, non-invasive biological imaging technique capable of imaging both *in vitro* and *in vivo* at the depths of several hundred microns. The goal of the thesis work is to contribute towards a fiber based non-linear excitation fluorescence microscopy system that we plan to build for our lab, which would later on be integrated with the OCT imaging setup and the DIC microscope. This thesis work involves filling in the key components in the microscopy system. These key components are; femtosecond pulse diagnosis, study of dispersion in optical media, dispersion free femtosecond pulse delivery and design and construction of an experimental multi-photon imaging setup which would be used for imaging biological samples. An interferometric autocorrelator was designed, built and interfaced with the computer for diagnosis of femtosecond laser pulses. In order to quantify the dispersion in optical fibers which are common choice for flexible delivery of light, a mathematical simulation was created. The results from the simulation indicated that optical fibers could not be used as the means to deliver ultrashort laser pulses for non-linear excitation fluorescence microscopy application. For the purpose of flexible delivery of ultrashort pulses as well as preserving their ultrashort temporal profile, hollow core photonic bandgap fiber (PCF)

was chosen and characterized. In the last part of the thesis work, an experimental setup of a two-photon excitation fluorescence microscope was designed and built with a flexible delivery setup and laser beam diagnosis setup.

TABLE OF CONTENTS

LIST OF FIGURES

LIST OF TABLES

x

CHAPTER 1

INTRODUCTION

1.1 Background

Two-photon fluorescence microscopy (TPFM) is a high resolution non-invasive biological imaging technique that can be used to selectively image cellular and extracellular matrix activity within in highly scattering tissues at the depths of several hundred microns [1] [2]. Although there are other optical techniques like confocal microscopy that provide comparable resolution to TPFM, TPFM is the technique of choice due to its deeper tissue penetration and reduced phototoxicity.

In 1990 when Denk and Webb introduced two-photon scanning fluorescence microscopy for the first time [3], they demonstrated the potential of imaging two-photon excitation fluorescence in a scanning microscope with *ultrashort pulsed lasers*. Due to the nonlinear nature of the excitation, the inherent confocality and the longer wavelengths of light used, this has become the technique of choice for high-resolution biological imaging[4].

Two-photon microscopy nowadays is being widely used for research in the following four areas:

1. Neurobiology[5],[6],[7],[8]

2. Embryology[9],[10],[11]

3. Dermatology[12],[13]

4. Optical Biopsy[14]

1.1.1 Requisites for two-photon excitation

Two-photon excitation of any molecule is related to the absorption of two long wavelength excitation photons simultaneous in space and time. The probability of two-photon absorption by a molecule can be mathematically expressed as [2]:

$$n_2 = \frac{(P_{avg})^2 \delta_2 \pi^2 (NA)^4}{\tau_p f_p^2 (hc\lambda)^2} \qquad (1.1)$$

where,

P_{avg} is the average power of the laser pulse

f_p is the repetition rate of the laser

τ_p is the laser pulse width

λ wavelength of light

NA is the numerical aperture of the objective lens used for focusing light

δ_2 is the two-photon absorption cross-section

The mathematical expression shows that the probability two-photon absorption of photons is directly proportional to the average power of the pulse and inversely proportional to its temporal width. When imaging cells and tissues it is needed to maintain low average power levels (5-10mW) to avoid cell and tissue damage which puts a lower limit on n_2. The other option to increase n_2 is to decrease τ_p. Thus, two photon excitation sources which produce temporally confined excitations pulses (i.e., ultrashort laser pulses) with required peak powers for efficient two-photon absorption (maintaining low average power) are requisites for a two-photon fluorescence microscopy system.

1.2 Ultrashort Laser Pulses

In physics, the term 'ultrafast' describes events that occur in a time duration equal to or shorter than picosecond ($10^{-12}sec$). With time the lowest laser pulse durations have drastically reduced from picoseconds (10^{-12}) to femtoseconds (10^{-18}) and now to attoseconds (10^{-18}). The shortest pulse width reported till date is in attosecond regime [15].

The main reason why ultrashort laser pulses are finding increasing application in biology and medicine is that these pulses have emerged as a unique tool for the study of ultrafast dynamics associated with light-matter interaction. The interaction of these pulses with matter at molecular, cellular and tissue level provides us with valuable chemical, physiological and structural information. Currently, ultrashort laser pulses are being used for various applications ranging from study of femtosecond dynamics of electrons in solids [16] to observing chemical reactions(femtochemistry)[17] [18] to non-linear microscopy [19] [20].
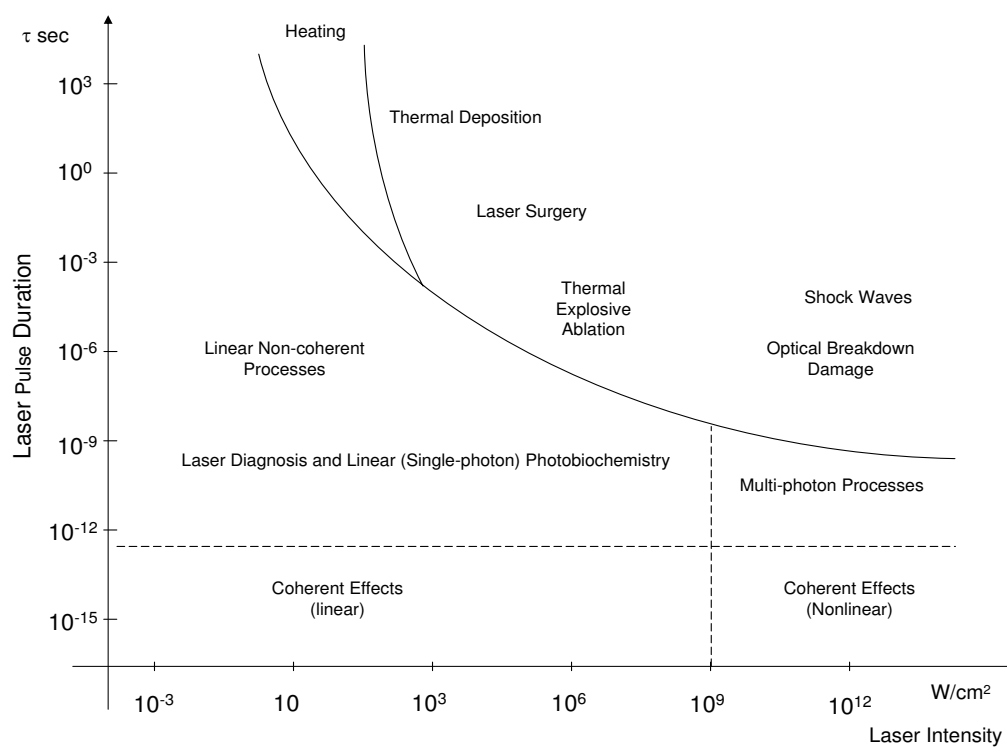
Figure 1.1 Various regimes of laser pulse interaction with tissues

Figure from Biomedical Optical Instrumentation and Laser-Assisted Biotechnology, Kluwer Academic Publishers 1996, Netherlands

1.3 Motivation

The goal of the thesis work is to contribute towards a fiber based non-linear excitation fluorescence microscopy system that we plan to build for our lab, which would later on be integrated with the OCT imaging setup and the DIC microscope. This thesis work involves finishing the required ground work for setting up the microscopy system as illustrated in the figure 1.2.

Pulsed laser light is the basic building block of all the optical imaging setups that are currently being used in our lab. The laser that we use is a Ti:Sapphire which can operate in the wavelength region $700nm - 1100nm$. The laser is capable of emitting both continuous output beam and pulsed output (modelocked). And, periodic trains of ultrashort laser pulses with durations less than picosecond ($10^{-12}sec$) are generated by modelocking of the laser source.
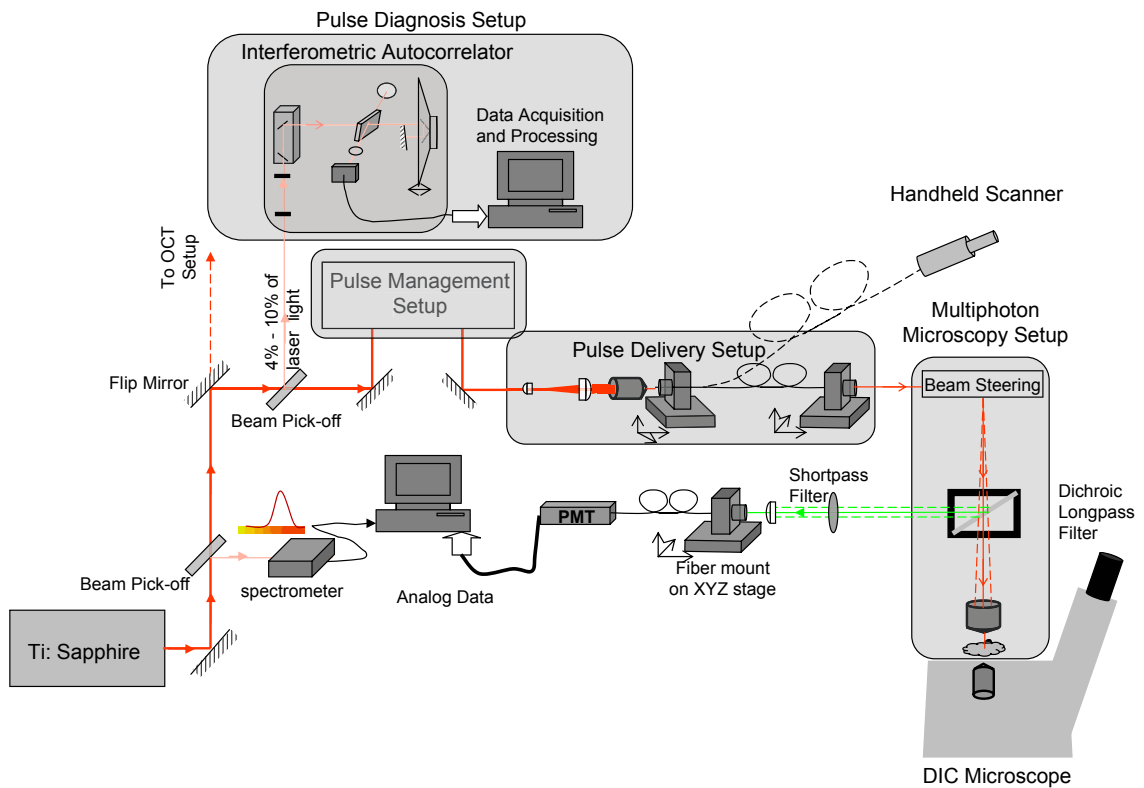
Figure 1.2 Vision of Multiphoton Microscopy System

Since the temporal profile of the laser pulse plays a vital role in the phenomenon of two-photon excitation, it was crucial to to monitor this parameter. The optoelectronic setup that is commonly used to monitor the temporal profile of the pulse is an interferometric autocorrelator which was designed and built with motive of pulse temporal characterization in real-time for their effective usage.

Our next undertaking was the flexible delivery of ultrashort pulses to the desired application; imaging, microscopy, nano-surgery etc. The most common means of flexible delivery of laser pulses is an optical fiber which are made up of optically dispersive material. To quantify the dispersion in optical media a mathematical simulation was created. Using this simulation we studied the dispersion of a laser pulse when it propagates through a given dispersive media of a given length. Using the model we did a comparative study the propagation of a chirped and un-chirped pulse through a dispersive media. Mathematical simulation such as this holds a considerable practical significance as the subject of pulse propagation is of great importance in the study of ultrashort pulses and their propagation.

The study of pulse propagation in dispersive media indicated that ultrashort pulses undergo temporal dispersion so significant that ultrashort pulses no longer remain ultrashort. The short temporal profile is the very property of the laser pulses which makes them viable for their application in multiphoton excitation fluorescence. This motivated us to assemble a setup for flexible delivery of the ultrashort pulses with minimum dispersion. For this purpose we chose a hollow core photonic crystal fiber (PCF). We also characterized the PCF by performing experiments to compare input-output pulsewidth, input-output power and input-output spectrum of the fiber.

The final task was to design and build an experimental two-photon imaging setup which could be used for the purpose of imaging of biological samples.

1.4 Specific Aims

The primary objective of the thesis work was to simultaneously monitor the laser pulse characteristics and deliver them to be used for two-photon application. The thesis work is divided into three segments:

1. Femtosecond pulse characterization
2. Femtosecond pulse delivery
3. Designing and building a two-photon imaging setup

The specific aims of the research work were:

1. Build an Interferometric Autocorrelator to characterize the temporal profile of ultrashort laser pulses.
2. Simulate a pulse propagation in a dispersive media.
3. Build and characterize a dispersion free (or minimum dispersion) flexible delivery system for ultrashort pulses.
4. Design and build a two-photon imaging setup for imaging biological samples.

1.5 Organization of thesis

This section gives a brief overview of the research work done towards the thesis and the motivation behind the work. It also enumerates the specific aims of the research work.

Chapter 2 details the principle, instrumentation concepts and working of the interferometric autocorrelator that was built as a part of the project. In addition it presents the application of the autocorrelator in pulse diagnosis and PCF characterization. The chapter also explains the software module programmed in LabVIEW to interface NI 6111 S-series DAQ card which acquires autocorrelation signal from the homebuilt detector.

Chapter 3 discusses the background of pulse propagation in a dispersive media and the mathematical simulation created to study the same. One of the sections in this chapter covers the study on pulse dispersion as a function of length of the four dispersive media (BK7, Fused Silica, SF5 and SF11) that are commonly used to make

optical components. The chapter discusses the propagation of chirped and un-chirped pulses through a dispersive media.

Chapter 4 describes the photonic crystal fiber based dispersion free delivery system. The chapter also includes the characterization of the system

Chapter 5 give a comprehensive review of the principle of non-linear excitation fluorescence and how ultrashort pulses induce non-linear excitation in matter. The chapter also discusses an experimental setup that was designed and built for two-photon excitation fluorescence imaging.

Chapter 6 discusses the future work for the completion of the MPM vision.

Chapters 2, 3 and 5 conclude with a discussion on the scope of improvements of the systems that were designed and built.

FEMTOSECOND LASER PULSE DIAGNOSIS

2.1 Ultrashort Laser Pulse Diagnostics

Before ultrashort pulses are used for any applications, it is necessary to characterize these pulses for their effective usage. The parameters of an ultrashort pulse one needs to analyze carefully are [21]:

- Energy in each pulse or average power
- Shape, temporal width and spectrum of the laser pulse

Measurement of the temporal profile of an ultrashort pulse is challenging because of a variety of limitations of the conventional; pure electronic methods. And, this chapter discusses the optoelectronic setup that was designed and built to measure these ultrashort pulses.
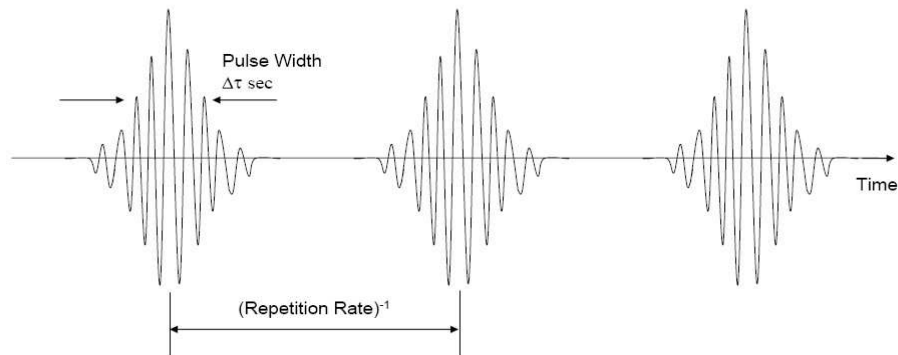
Figure 2.1 Output of Pulsed Laser

Now the question that arises is if these pulses have ultrashort temporal width, how can these fast temporal events be measured? To measure time of the order of 10^{-15}, we need a temporal resolution higher than that of the ultrashort pulse that has to be

measured. Even with a fast photodiode the time resolution that can be achieved is $\approx 8ps$ which cannot fulfill the needs of ultrashort pulse characterization in the femtosecond regime. The solution to this problem is; to measure the ultrashort pulse against itself. This method is known as autocorrelation.

2.1.1 Interferometric Autocorrelation

2.1.1.1 Theoretical Background

An autocorrelator is an optical setup that practically implements the mathematical expression given below:

$$I_A(\tau) \propto \int_{-\infty}^{\infty} I_1(t)I_1(t - \tau)dt \tag{2.1}$$

where,

I_1 is the light intensity of the input pulse

$I_A(\tau)$ is the autocorrelation of the input pulse

τ is the lag
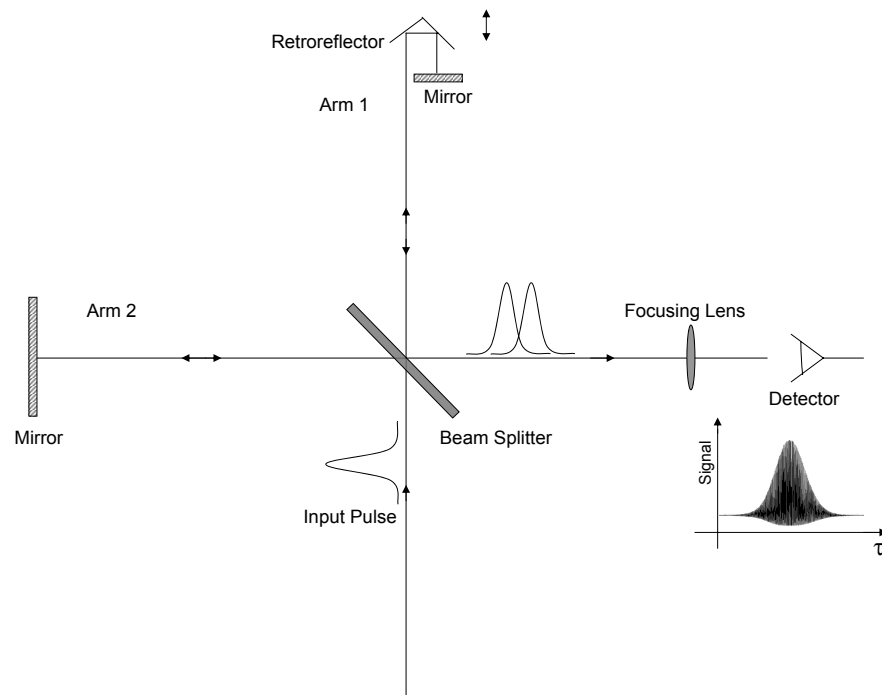
Figure 2.2 Schematic Diagram of an Autocorrelator

The schematic diagram of an Interferometric Autocorrelator is as shown in the figure 2.2. As can be seen in figure 2.2, the incoming pulsed laser beam is divided in to two identical parts using a 50:50 beam-splitter. These two parts travel a certain distance and retrace the same path . When the difference between path lengths traced by these two pulses is zero, maximum overlap is seen. And, the lag in the equation is mismatch between the two paths that is obtained by scanning one of the arms of the autocorrelator.

Assuming a gaussian shaped pulse was the input to the autocorrelator:

$$E(t) = e^{-\frac{1}{2}(\frac{t}{\tau_p})^2(1+i\beta)} \tag{2.2}$$

where,

τ_p is the FWHM of the input pulse

β is the chirp of the pule

The Interferometric autocorrelation signal for the incoming pulse (equation 2.2) is:

$$I_{IAC}(\tau) = 1 + \left\{ 2 + e^{-\frac{\beta^2}{2}(\frac{t}{\tau_p})^2} cos(2\omega_0\tau) \right\} e^{-\frac{1}{2}(\frac{t}{\tau_p})^2} + 4e^{-\frac{3+\beta^2}{8}(\frac{t}{\tau_p})^2} cos\left\{ \frac{\beta}{4}\left(\frac{t}{\tau_p}^2\right) \right\} cos(\omega_0\tau) \tag{2.3}$$

2.1.2 Autocorrelator

In this section we will discuss the architecture of the autocorrelator. The autocorrelator setup is built on an optical breadboard with the dimensions $12in \times 10in \times 8\frac{1}{2}in$, figure 2.3 shows the top view of the optical setup of the autocorrelator. The incoming laser beam is at a height of $3\frac{1}{4}in$, but the desirable height of the laser beam is $5in$. To translate the beam to the desired height a periscope setup is used as shown in the figure 2.3. The input laser beam is made to pass through a pinhole assembly which is used not only to spatially filter the incoming beam, but also makes the autocorrelator setup easy to install.
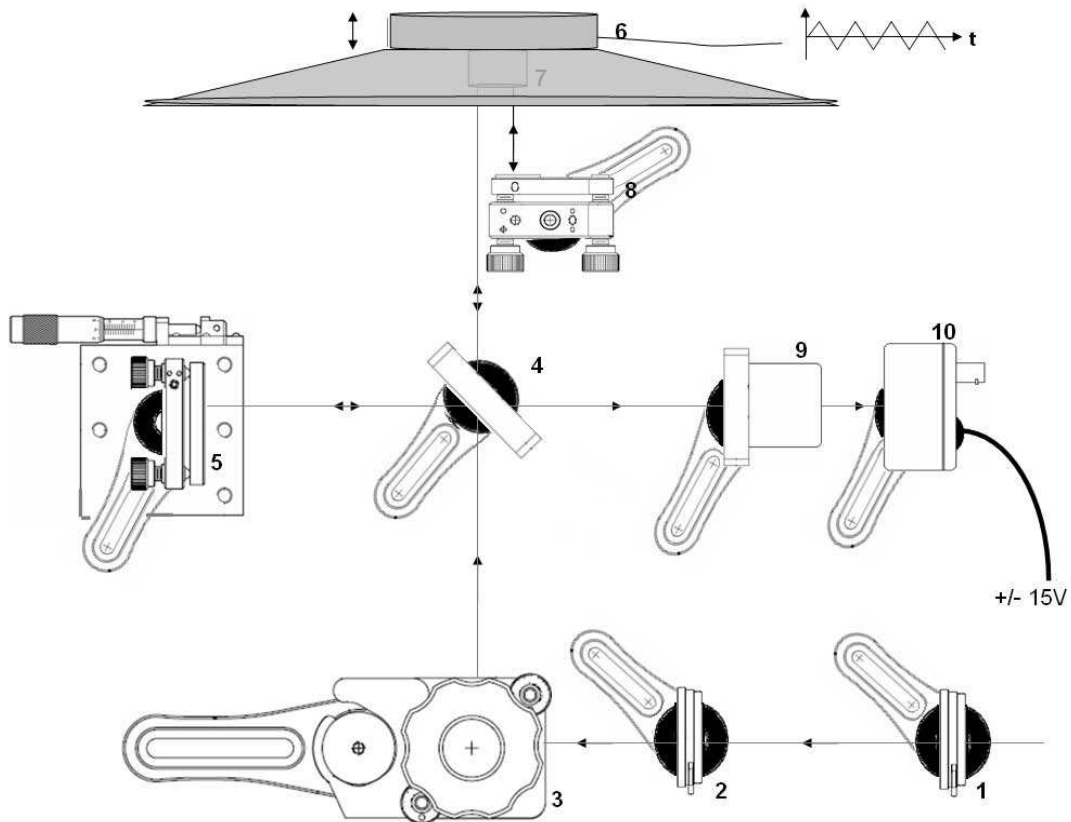
Figure 2.3 Top view of the autocorrelator optical setup

1,2-Pinhole Assembly, 3-Periscope, 4-Beam-splitter, 5-Mirror, 6-Speaker, 7-Retroreflector, 8-Mirror, 9-Lens, 10-Detector

2.1.2.1   The Beam-splitter

Beam-splitter is an optical element which allows a part of the electromagnetic wave and reflecting the other part. Any simple dielectric layer can serve as a beam-splitter. Beam-splitters are made of substrate coated with a dielectric layer with the splitting occurring at dielectric layer. The beam-splitter used in the autocorrelator is an ultrafast laser beam-splitter (Newport 10RQ00UB.2). These beam-splitters are specially designed to minimize pulse dispersion and maximize bandwidth for beam sampling and autocorrelation measurements of ultrafast laser pulses. The front surface is coated with a dielectric material which provides a 50/50 split at 45 angle of incidence for s-polarized

light from 700 to 950nm. A thin UV grade fused silica substrate, with l/10 wavefront distortion, is used to reduce pulse dispersion from the substrate material [22].
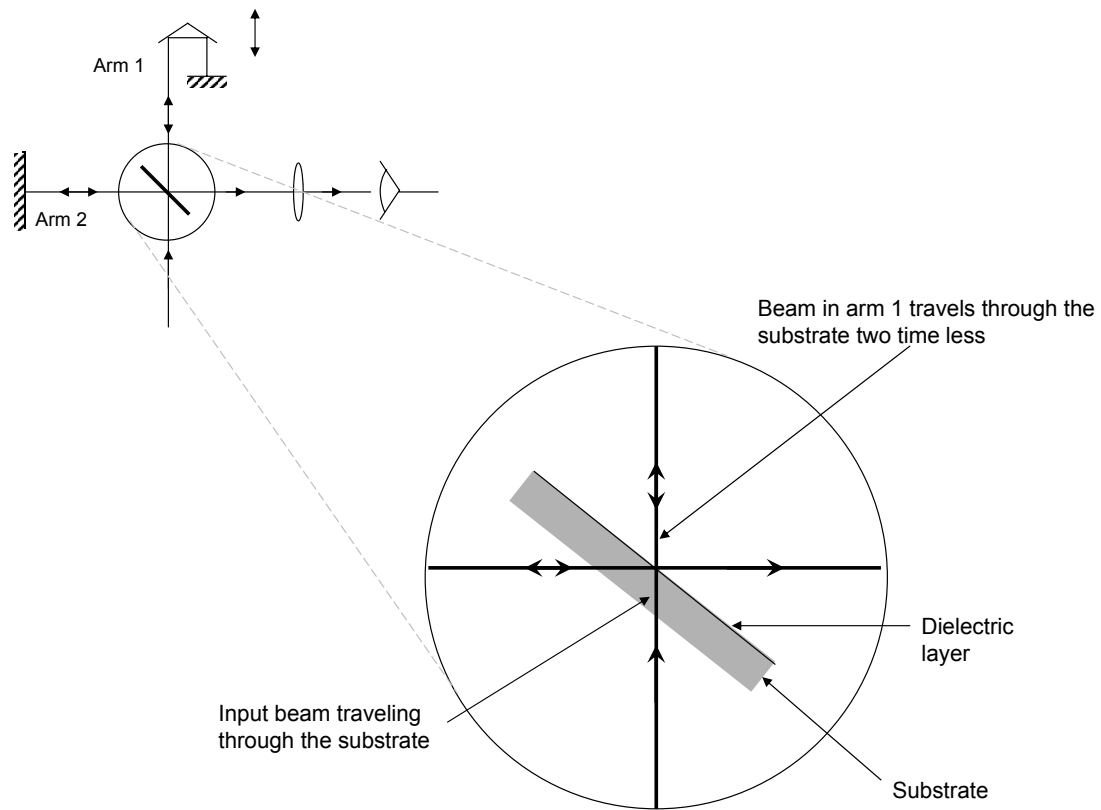
Figure 2.4 Beam-splitter

When a beam is split using a beam-splitter there are certain issues that need to be addressed. As can be seen in the figure 2.4 the beam in one arm travels through the (UV fused silica) substrate two times less than the beam in the other arm. This will cause the dispersion imbalance between the both the arms which can problems. Our autocorrelator does not address this problem. The suggested solution for this problem is that an additional substrate can be added in the path 1 which balances out both the arms in the autocorrelator. Another solution to this problem is to cut the beam-splitter

in half and flip the halves such that the dielectric layers face the opposite directions [23]. This point leaves a scope for improvement of our autocorrelator.

2.1.2.2 Scanning Retro-reflector

Retroflectors are constructed of three reflecting first surface mirrors into a corner of a cube i.e., all these surfaces are perpendicular to each other which makes these totally insensitive to position and movement. The result is that parallel incident light will be reflected with great accuracy back to the light source, regardless of the angle of incidence. Thus retroreflector is used in the scanning arm of the autocorrelator instead of a mirror. The retroreflector used of our application is a hollow retroreflector made of pyrex material with a gold coating designed for 650 nm with a clear aperture of 12.7 mm (Edmund Optics NT46-181) [24]. The retroreflector was scanned by mounting it on a speaker cone and the speaker was driven sinusoidally at 10 Hz using a function generator.

The path lengths of the two arms are matched by micrometer adjustments in the arm 2. When the path lengths in both the arms match up we get the autocorrelation signal. We can see two autocorrelation signals per oscillations as shown in the figure 2.5. The micrometer is adjusted such that autocorrelation signal is placed at the center of the scan of the retroreflector. This is the done to ensure that the acquired autocorrelation signal occurs in the linear scan region of the sinusoidal scan of the retroreflector.

2.1.2.3 Photo-detector - Two-Photon Absorption

The photo-detector used for detection of the autocorrelation signal is a home built detector. The photodiode used to build the photodetector is a GaAsP-photodiode (Hamamatsu G1116). The spectral response of the photodiode is from 300 nm to 680 nm. The input laser pulses are in the wavelength range 700 nm to 900 nm. These pulses are detected by the photodiode due to two-photon absorption of these pulses. Thus, from the detector point of view, the autocorrelator can be used for wavelength range from 600
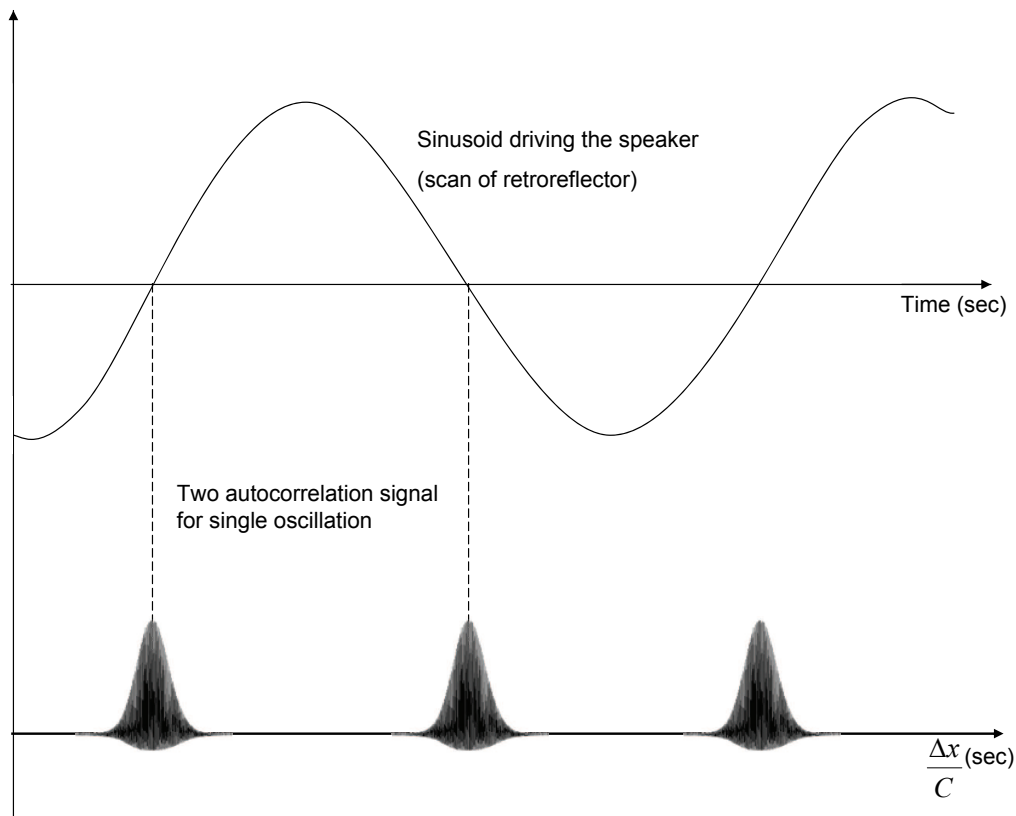
Figure 2.5 Single scan of retroreflector

nm to 1360 nm. The electrical circuit of the homebuilt photodetector is as shown in the figure 2.10.

2.1.3 Calibration and Measurement

NI LabVIEW is an open environment designed to make interfacing with any measurement hardware simple [25]. For interfacing the output of the photodetector with the computer LabVIEW 7.1 was used. National Instruments DAQ card 6111 was used to acquire the interferometric autocorrelation signal (IAC) from the autocorrelator. This section explains the LabVIEW module designed and programmed to acquire and interpret the autocorrelation signal. There are two VIs, Calibration and Measurement, discussed in this section.
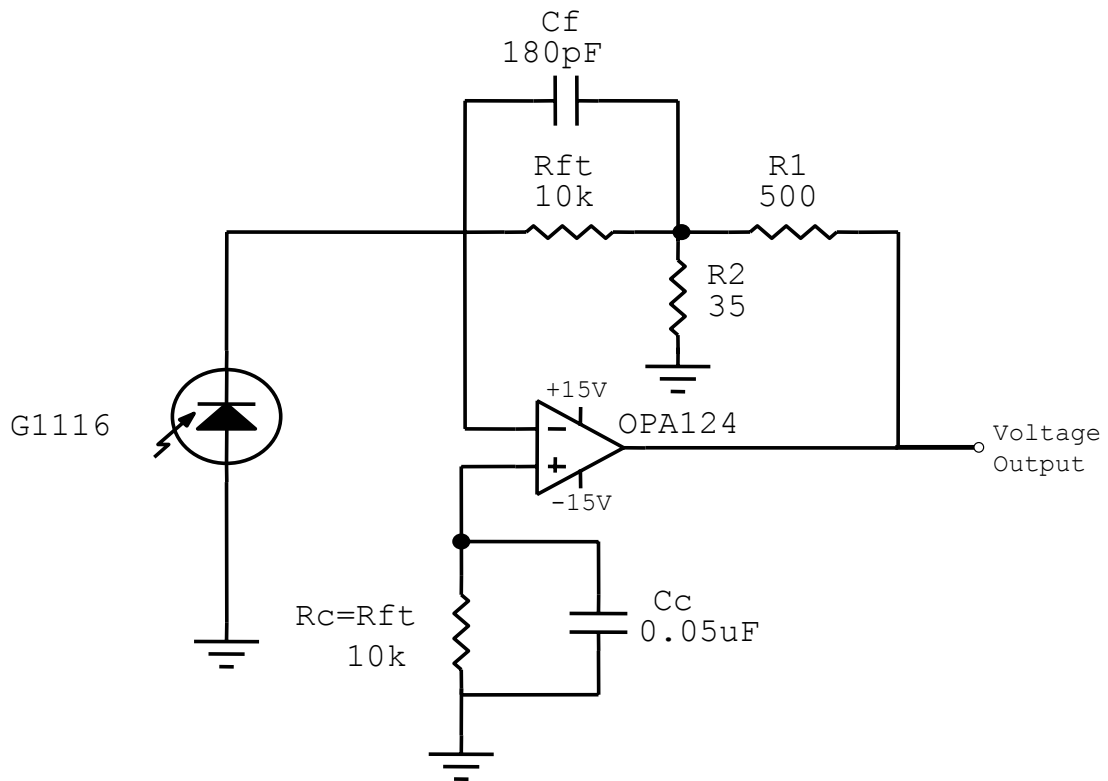
Figure 2.6 Photodetector Circuit

2.1.3.1 Calibration

The arm 1 of the autocorrelator is the scanning arm. The scanning motion of this arm is obtained by feeding the speaker with a sinusoidal signal from the signal generator. This scanning motion of the speaker introduces the lag (equation 2.1) between the two autocorrelating pulses in the optical setup. The autocorrelation signal is obtained only when the path length difference between the two arms is less than $\frac{\lambda}{2}$, where λ is the wavelength of the laser pulses. This is referred to as path lengths of the both arms to be matched.

The signal from the photo detector is first acquired using the 'Calibration VI' for calibrating the output. The snapshot of the calibration.vi is as shown in the figure 2.7 The data acquisition is triggered by the trigger output signal from the signal generator that drives the scanning arm. The IAC signal is acquired at a sampling rate of 2 MHz
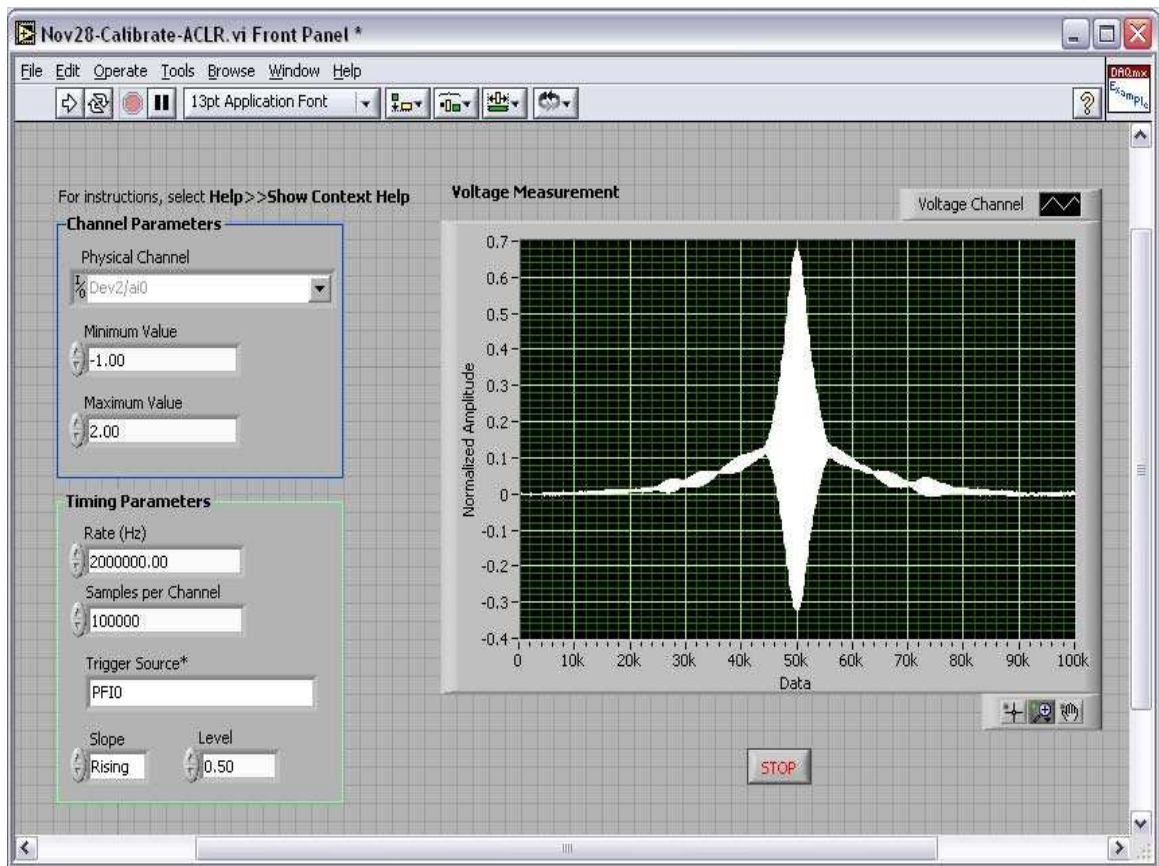
Figure 2.7 Snapshot of Calibration VI

and the samples per channels that are acquired are 100000 samples. This implies that the data is acquired for 0.05 sec (Samples per channel / Sampling Rate) after the trigger is detected. Single oscillation of the sinusoidal input results in forward and backward scan of the retroreflector. Each scan (forward and backward) results in one IAC signal. The micrometer in the arm 1 is adjusted such that the IAC signal falls in the center of the forward and backward scan of the retroreflector. This adjustment can be done by simultaneously acquiring the signal generator output and the triggered IAC signal. This adjustment also ensures that the IAC signal falls in the linear region of the scan.

The data for calibration or measurement is acquired only for a single scan (forward or backward), which means that 100000 samples represent single forward or backward scan. To relate the scan dimension and the number of samples, the micrometer in the arm 1 of the autocorrelator is moved (Δx units), which results the IAC signal to shift

(Δs samples) on the VI display. Therefore, each sample in the data represents a scan dimension of

$$\Delta z = \frac{\Delta x}{\Delta s} \tag{2.4}$$

This scan dimension is related to the change in delay or lag $\Delta \tau$ by

$$\Delta \tau = \frac{\Delta z}{c} \tag{2.5}$$

where, c is the speed of light.

For example, if $\Delta x = 6 \times 10^{-5}$ m and $\Delta s = 10000$ samples then, $\Delta z = 6 \times 10^{-9}$ m. This scan dimension means that the pulse delay is changing $\Delta \tau = 0.02 fsec$ with each acquired sample.

This calibration protocol is followed every time the autocorrelator is used. Δz is one of the parameters that is stored in the header information of the binary file which contains the acquired IAC signal.

2.1.3.2 Measurement

Two measurement VIs were made for the purpose of measurement of FWHM τ_{IAC} of the IAC signal which in turn is related to the input pulsewidth τ_{ip} by the equation $\frac{\tau_{ip}}{\tau_{IAC}} = \frac{1}{\sqrt{2}}$ for a gaussian input pulse. The first VI (figure 2.8) (acquire and store binary VI) acquires the IAC signal and stores it as a binary file with head information. The header information contains the following parameters:

- Date and Time
- Maximum Voltage in mV
- Minimum Voltage in mV
- Sampling Rate in Hz
- Samples per Channel
- Scan Dimension in 10^{-5} m
- Scans to Average
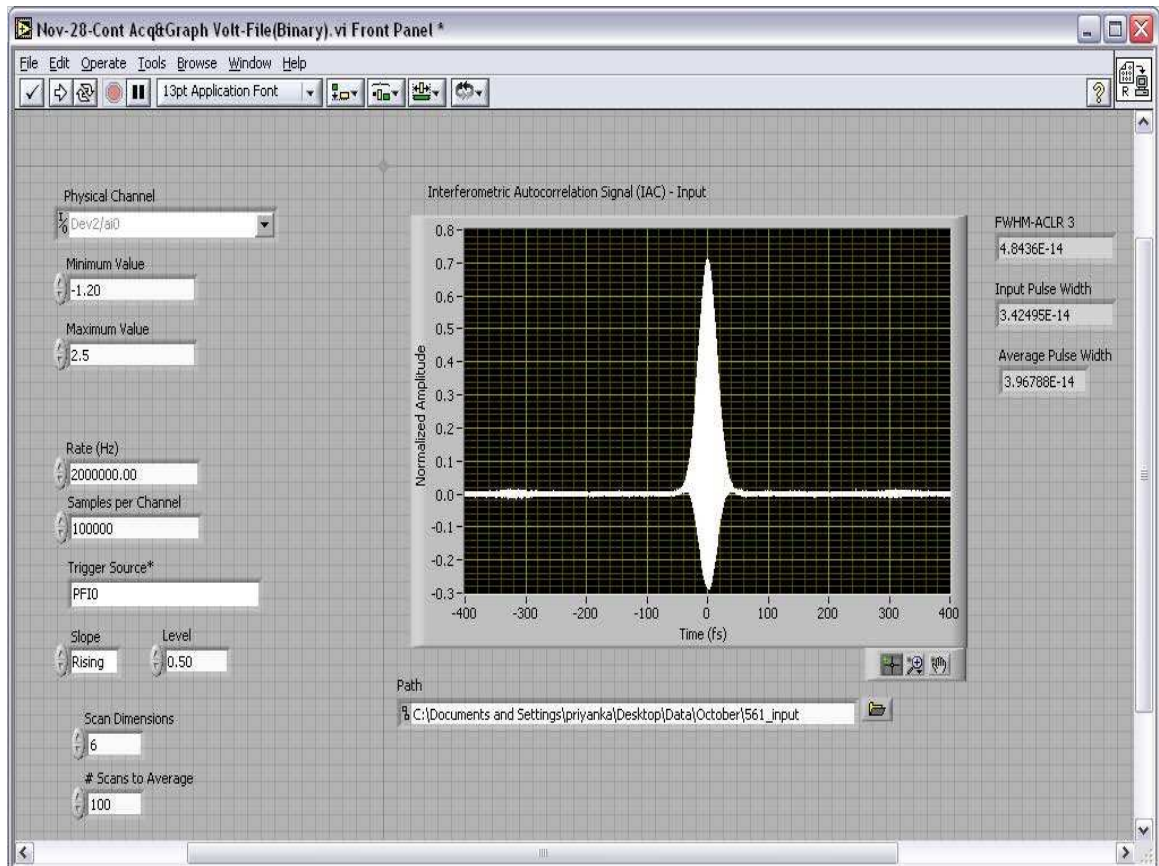
Figure 2.8 Snapshot of Acquire and Store Binary - VI

Scans to average specifies the number of averages that is used for computing the pulse width of the input pulse. And, the acquisition of data stops after the number of averages are completed. The second VI shown in the figure 2.9 (read binary VI) does not acquire the IAC signal but read the signal from the binary files stored by 'acquire and store binary VI'. The header information in the binary files is extracted to analyze the IAC signal and calculate the pulse width.

2.2   Scope of Improvement

The scope of improvements for the autocorrelator lie not only in the design but also in the components that were used to build it. There can be various other designs that can be used for the autocorrelation of the femtosecond pulses which have their respective advantages and disadvantages. The components that can improve the performance of
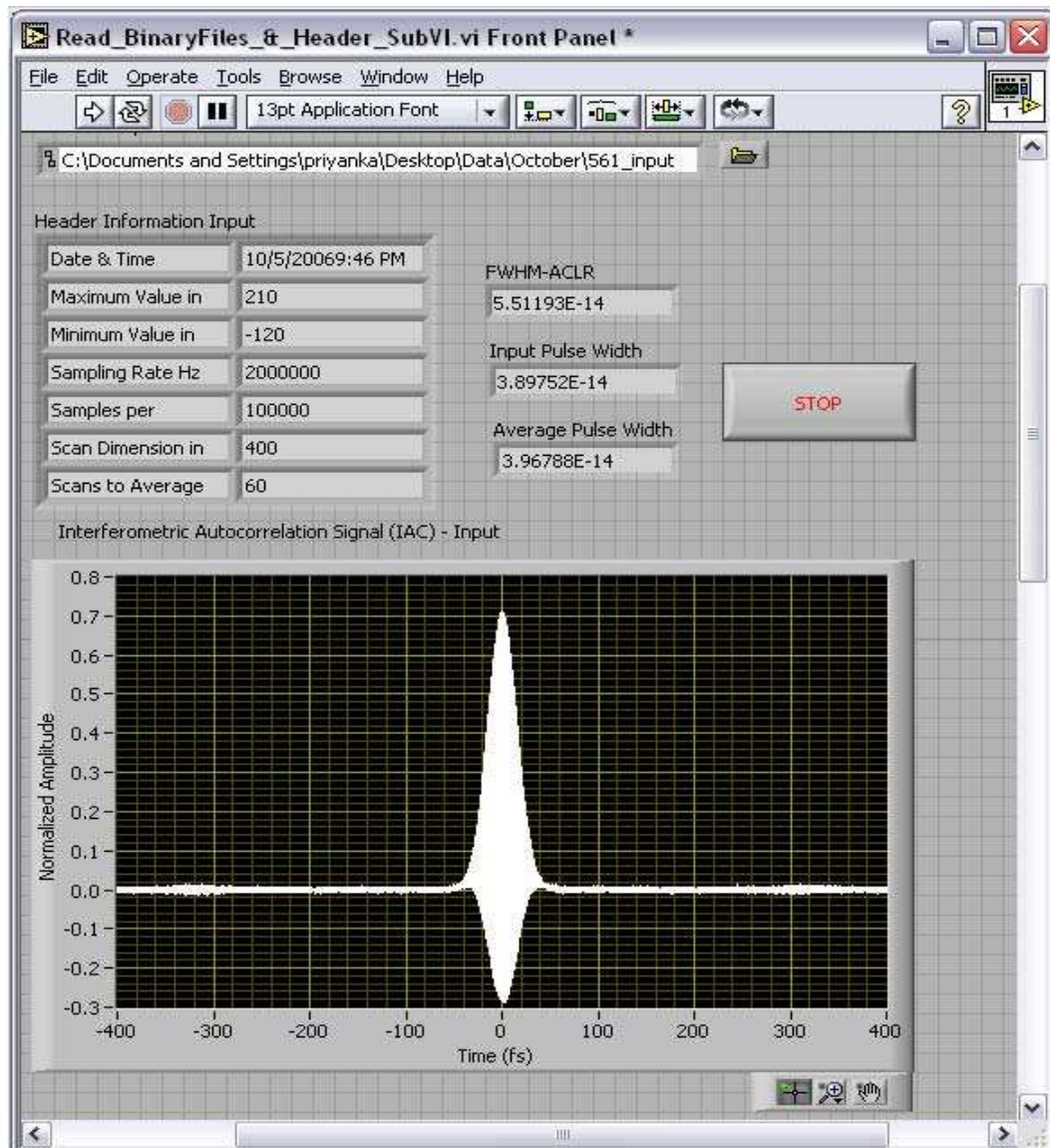
Figure 2.9 Snapshot of Read Binary VI

the autocorrelator are the beam-splitter and the scanning setup. A scanner with a better response at lower frequencies will prove to be a plus factor in accuracy and repeatability of measurement. The accuracy in pulse width measurement can also be improved by using iterative methods to curve fit the acquired IAC signal in the standard IAC equation.These methods are computationally intensive and time consuming. We tried to implement MOSAIC (modified-spectrum autointerferometric correlation) technique [?] for our application which needs further work.

Figure 2.10 Flow chart showing acquisition and storing of IAC signal

CHAPTER 3

FEMTOSECOND PULSE PROPAGATION IN DISPERSIVE MEDIA

Mode-locked lasers are capable of producing extraordinarily temporally short optical pulses with high average power. In the previous chapter we discussed about how the temporally short laser pulses can be characterized using an optoelectronic setup.

Next task was to build a fiber based light delivery to the multiphoton imaging setup. The most common flexible delivery of light is through optical fibers which are made of optically dispersive material. Our goal of the light delivery system is not only the flexible delivery of light pulses but also to preserve the ultrashort temporal profile of the pulse when it propagated through this delivery system. This lead us to study and quantify the effects of various dispersive material on a propagating ultrashort pulse. Another question that needed to be answered was, will these effects act adversely on the application of ultrashort pulses in multiphoton imaging of biological systems.

The study of pulse propagation also holds a considerable practical importance in analyzing optical systems like laser amplifiers (i.e., active propagation systems), optical fibers and other passive propagation systems. This chapter starts with an introduction to fundamentals of pulse propagation in linear dispersive systems which covers concepts of group and phase velocities. Then, the chapter discusses the mathematical simulation of dispersion in a linear dispersive system.

3.1 Theoretical Background

The time representation of real electric field corresponding to a monochromatic plane wave is given by [21]:

$$E(t) = Re\left(E_0 e^{i\omega_0 t} e^{ib(t)}\right) \tag{3.1}$$

where,

E_0 is Intensity of the oscillating electric field of light

ω_0 is frequency of oscillation corresponding to wavelength of light.

$b(t)$ is the phase function
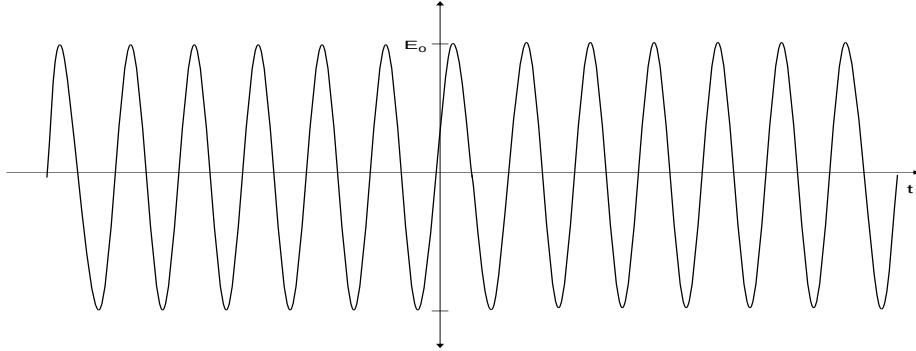
Figure 3.1 Schematic representation of electric field of monochromatic plane wave

Since we were interested in studying the dispersion of ultrashort pulses, the pulse shape assumed for the mathematical simulation was a gaussian pulse as shown in the figure 3.2. The mathematical representation of a light pulse with a complex gaussian envelope with a magnitude unity is [26]:

$$E(t) = e^{(-at^2)}e^{i(\omega_0 t + b(t))} = e^{(-\Gamma t^2)}e^{i\omega_0(t)} \tag{3.2}$$

The complex gaussian parameter describing this pulse is given by [26]

$$\Gamma \equiv a - ib \tag{3.3}$$

Also, full width at half maximum pulse width is defined by τ_p and is related to the parameter a by [26]:

$$\tau_p = 2\sqrt{\frac{ln2}{a}} \tag{3.4}$$

The gaussian pulse spectrum is given by [26]:

$$\tilde{E}(\omega) = F\left\{E(t)\right\} = F\left\{e^{(-\Gamma t^2 + i\omega_0 t)}\right\} \Rightarrow e^{\frac{(-\omega - \omega_0)^2}{4\Gamma}} \tag{3.5}$$
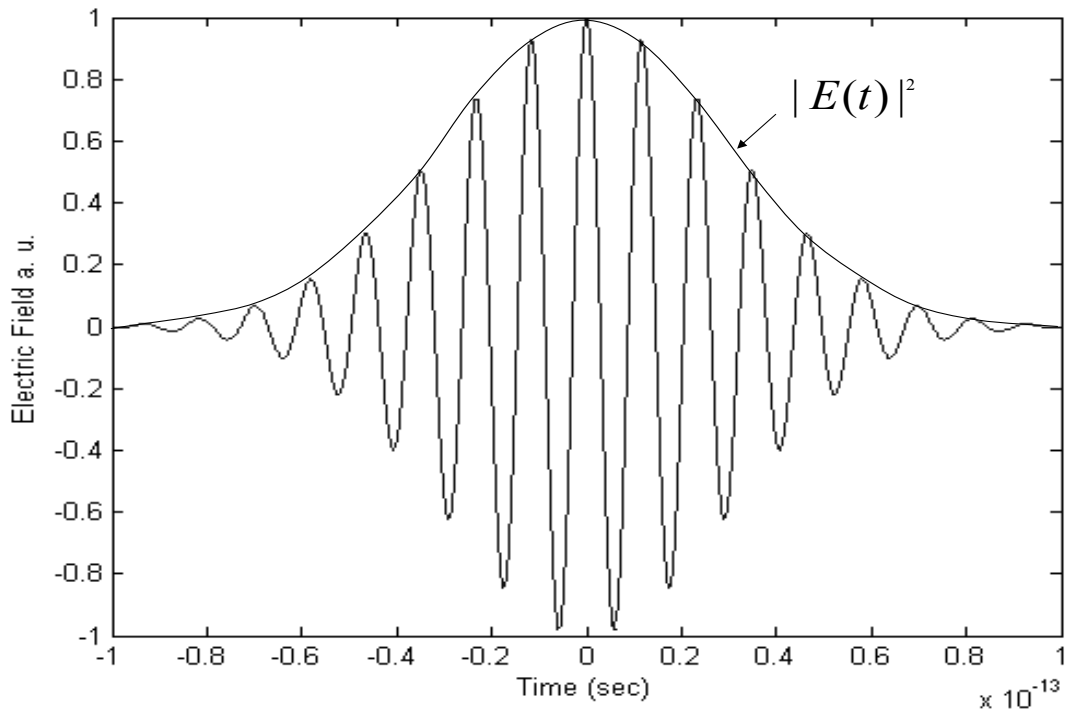
Figure 3.2 Schematic representation of electric field of a gaussian light pulse

The figure below illustrates the effects of propagation of light pulses through a dispersive media.

Now consider a dispersive wave propagating linear system like an optical fiber or any lens. The propagation constant of such a medium with permeability μ and permitivitty ϵ can be written as:

$$\beta \equiv \omega\sqrt{\mu\epsilon} \tag{3.6}$$

If μ and ϵ are constants i.e., if they do not vary with the wavelength of the light pulse then:

$$\beta = \frac{\omega}{c} \tag{3.7}$$

where, $c = \frac{1}{\mu\epsilon}$ If the dispersive material properties vary with change is wavelength of light propagating, then the propagation constant is a frequency dependent propagation factor and is given as:

$$\beta(\omega) = \frac{n(\omega)\omega_0}{C_o} \tag{3.8}$$
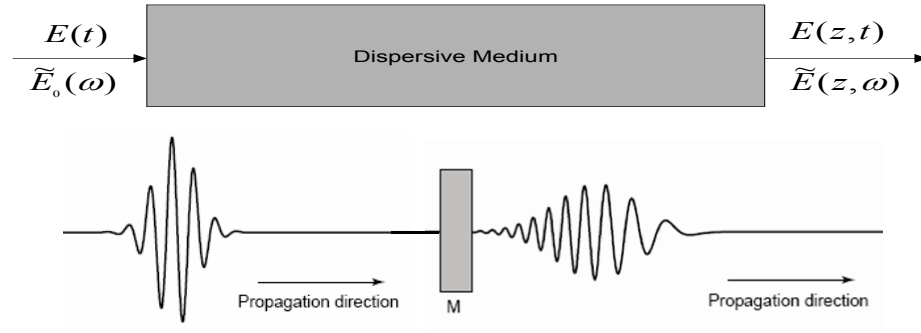
Figure 3.3 Modification of gaussian pulse spectrum

where,

$$C_0 = \frac{\lambda\omega}{2\pi}$$

$n(\omega)$ defines the refractive index of the dispersive media as a function of wavelength

In order to allow for a partial analytical calculation of propagation effects, the propagation factor is rewritten using a Taylor expansion as a function of the angular frequency assuming that $\Delta\omega << \omega_0$. Applying the Taylor expansion we get [21]:

$$\beta(\omega) = \beta(\omega_0) + \beta'(\omega - \omega_0) + \frac{\beta''}{2}(\omega - \omega_0)^2 + ... \quad (3.9)$$

where,

$$\beta' = \left(\frac{d\beta(\omega)}{d\omega}\right)_{\omega=\omega_0} \quad (3.10)$$

and

$$\beta'' = \left(\frac{d^2\beta(\omega)}{d\omega^2}\right)_{\omega=\omega_0} \quad (3.11)$$

When an optical pulse propagates a distance z through such medium (figure 3.3) its spectrum is modified as shown in the equation below [26]:

$$\tilde{E}(z,\omega) = \tilde{E}(\omega) \times e^{-i\beta(\omega)z}$$

$$\tilde{E}(z,\omega) = exp\left[-i\beta(\omega_0)z - i\beta' z \times (\omega - \omega_0) - \left(\frac{1}{4\Gamma_0 + \frac{i\beta'' z}{2}}\right) \times ((\omega - \omega_0))^2\right] \quad (3.12)$$

Taking an inverse Fourier transform of equation 3.12 we get a gaussian pulse of the form $e^{-\Gamma t^2}$, with a shift in time by $t - \beta' z$ [26]:

$$E(z,t) = e^{[i(\omega_0 t - \beta(\omega_0 z))]} \times e^{[-\Gamma(z) \times (t - \beta' z)^2]} \quad (3.13)$$

where,

$\Gamma(z)$ is the modified gaussian pulse parameter after traveling a distance z.

From the first exponent is the equation 3.13 it can be inferred that when the gaussian pulse propagates a through a dispersive length z the phase of the sinusoidal carrier with frequency ω_0 is delayed by a phase shift given by $\beta(\omega_0 z)$ which represents that there is a time delay between the input and the output pulse called *phase delay* is given by [26]:

$$t_\phi = \frac{z}{v_\phi(\omega_0)} = \frac{\beta(\omega_0)}{\omega_0} z \quad (3.14)$$

$v_\phi(\omega_0)$ *phase velocity*, in the equation 3.14 refers to the velocity at which the sinusoidal waves within the pulse envelope will appear to move forward given by [26]:

$$v_\phi(\omega_0) = \frac{z}{t_\phi} = \frac{\omega_0}{\beta(\omega_0)} \quad (3.15)$$

The second exponent in the equation 3.13 shows that the dispersed pulse with a modified gaussian pulse parameter $\Gamma(z)$ is also delayed by a time t_g called *group delay* which is given by [26]:

$$t_g = \frac{z}{v_g(\omega_0)} = \beta' z \quad (3.16)$$

$v_g(\omega_0)$ *group velocity* in the equation 3.17 refers to the velocity at which the pulse envelope appears to move forward given by [26]

$$v_g(\omega_0) = \left(\frac{1}{d\beta/d\omega}\right)_{\omega=\omega_0} = \left(\frac{d\omega}{d\beta}\right)_{\omega=\omega_0} \tag{3.17}$$

Analyzing the equation 3.13 it is understood that pulse dispersion depends on the element $\Gamma(z)$ which in turn depends on the second and higher order coefficients in the Taylor's expansion of propagation constant [26].

$$\frac{1}{\Gamma(z)} = \frac{1}{\Gamma} + 2i\beta''(\omega_0)z \tag{3.18}$$

3.2 Mathematical Model

In the previous section the mathematical background of gaussian pulse and its propagation was discussed. The next step towards simulating a mathematical model was to understand the about how the linear dispersive media effects the propagating light pulse. As can be understood from the equation 3.8 propagation constant $\beta(\omega)$ is dependent on refractive index of the dispersive medium.

In order to simulate a dispersive media Sellmeier's equation was used which is given as:

$$n^2(\lambda) = 1 + \frac{B_1\lambda^2}{\lambda^2 - C_1} + \frac{B_2\lambda^2}{\lambda^2 - C_2} + \frac{B_3\lambda^2}{\lambda^2 - C_3} \tag{3.19}$$

B_1, B_2, B_3, C_1, C_2 and C_3 are constants that define a particular material where wavelength λ is expressed in μm. For example, material constants for Schott BK7 are $B_1 = 1.03961212$, $B_2 = 0.231792344$, $B_3 = 1.01046945$, $C_1 = 6.00069867 \times 10^3$, $C_2 = 2.00179144 \times 10^{-2}$ and $C_3 = 1.03560653 \times 10^2$.

The wavelength dependence of refractive index was translated into angular frequency dependence using the relationship:

$$\lambda = \frac{2\pi C}{\omega} \tag{3.20}$$

where,

C is the speed of light in vacuum

The coefficients in the Taylor series expansion equation are calculated using the equation 3.8

$$\beta(\omega) = \frac{n(\omega)\omega_0}{C_o}$$

where, $C_0 = \frac{\lambda\omega}{2\pi}$

Differentiating the above equation 3.8 with respect to angular frequency ω we get:

$$\frac{d\beta}{d\omega} = \frac{1}{C_0}\left[n(\omega) + \omega\frac{dn}{d\omega}\right] \tag{3.21}$$

$$\frac{d^2\beta}{d\omega^2} = \frac{1}{C_0}\left[2\frac{dn}{d\omega} + \omega\frac{d^2n}{d\omega^2}\right] \tag{3.22}$$

$$\frac{d^3\beta}{d\omega^3} = \frac{1}{C_0}\left[3\frac{d^2n}{d\omega^2} + \omega\frac{d^3n}{d\omega^3}\right] \tag{3.23}$$

The higher order coefficients can be calculated by differentiating the lower orders. Since the higher order coefficients carry the pulse dispersion information the mathematical model includes the coefficients till the fourth order. The flow chart (figure 3.4) illustrates the approach of the simulation. The figure 3.5 shows the snapshot of the graphical user interface that was given to the simulated mathematical model.

3.3 Results and Analysis

Using the simulation the dispersive property of four common materials used for making optical components were studied. The four materials were :

- Fused Silica
- Schott BK7
- SF5
- SF11

In this study, light pulses with different pulse width ($10fs$ - $100fs$) were propagated through four different materials and the data was graphical represented as shown in the figure 3.6 - 3.9. As we can seen in all the four plots, the shorter the temporal width of
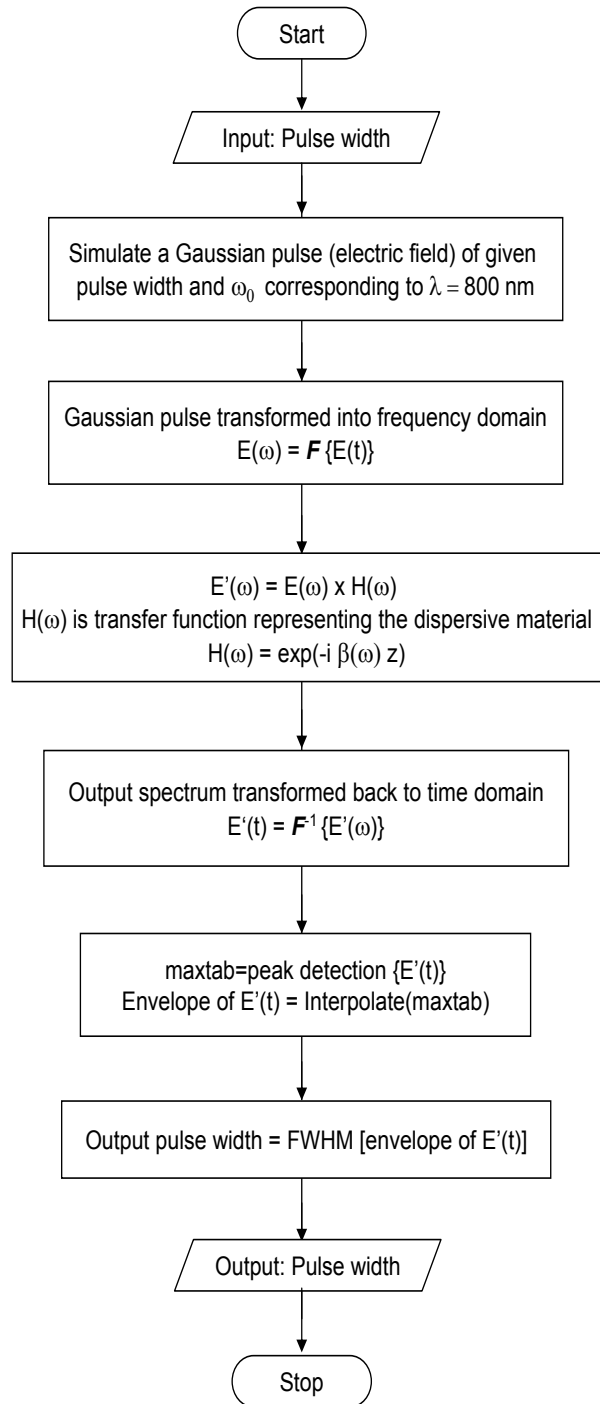
Figure 3.4 Flow chart for simulation
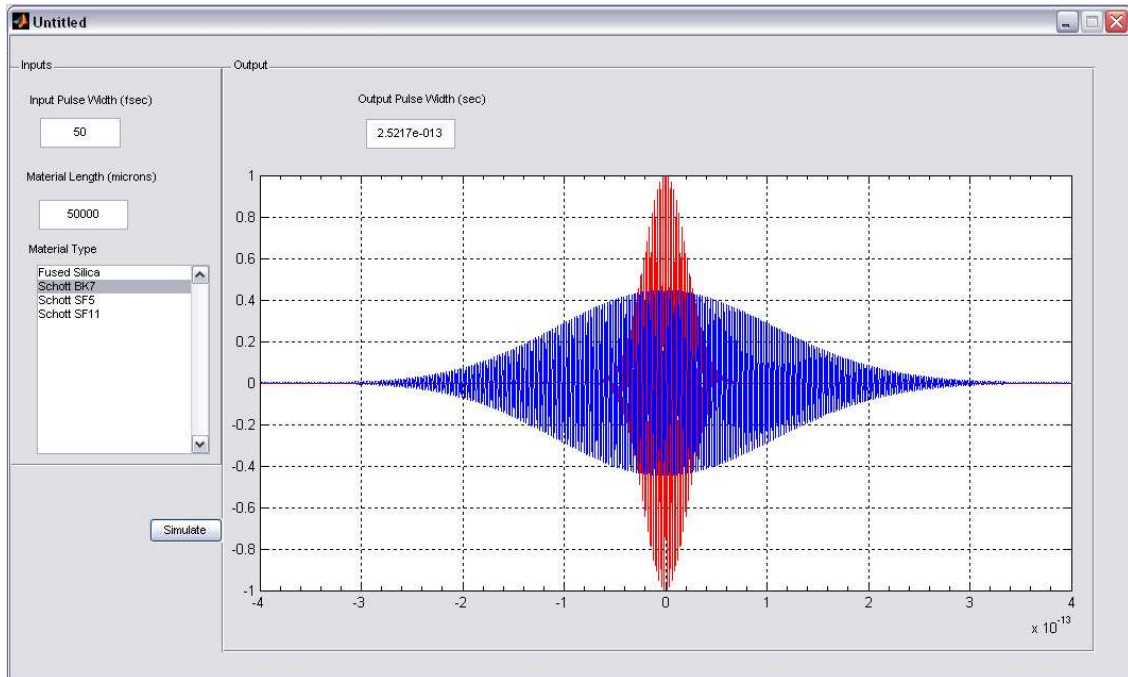
Figure 3.5 GUI for the Mathematical Model

the pulse the greater the dispersion of the pulse in propagating medium. The data also shows that the material SF11 disperses the light the most and Fused Silica the least (this is the reason fused silica is used as a substrate for beam-splitters and beam pickoffs).

The simulation was also used to study the effects of chirp on the dispersion. The results are tabulated in table 3.1   The results tell that a chirped pulse disperses more

Table 3.1 Effects of Chirp on Pulse Propagation

Input Pulse Width	Chirp	Dispersive Length	Output Pulse Width
10 fsec	No chirp	50mm BK7	1.374×10^{-12} sec
10 fsec	Chirped	50mm BK7	1.73×10^{-12} sec
50 fsec	No chirp	50mm BK7	2.521×10^{-13} sec
50 fsec	Chirped	50mm BK7	3.864×10^{-13} sec

in a propagating media compared to an un-chirped pulse. The shorter the pulsewidth of the chirped pulse, the higher the dispersion.

From the mathematical simulation it was concluded that use of optical fibers as a flexible pulse delivery system was not suitable for our application as our application demands the preservation of ultrashort temporal profile of the pulse.
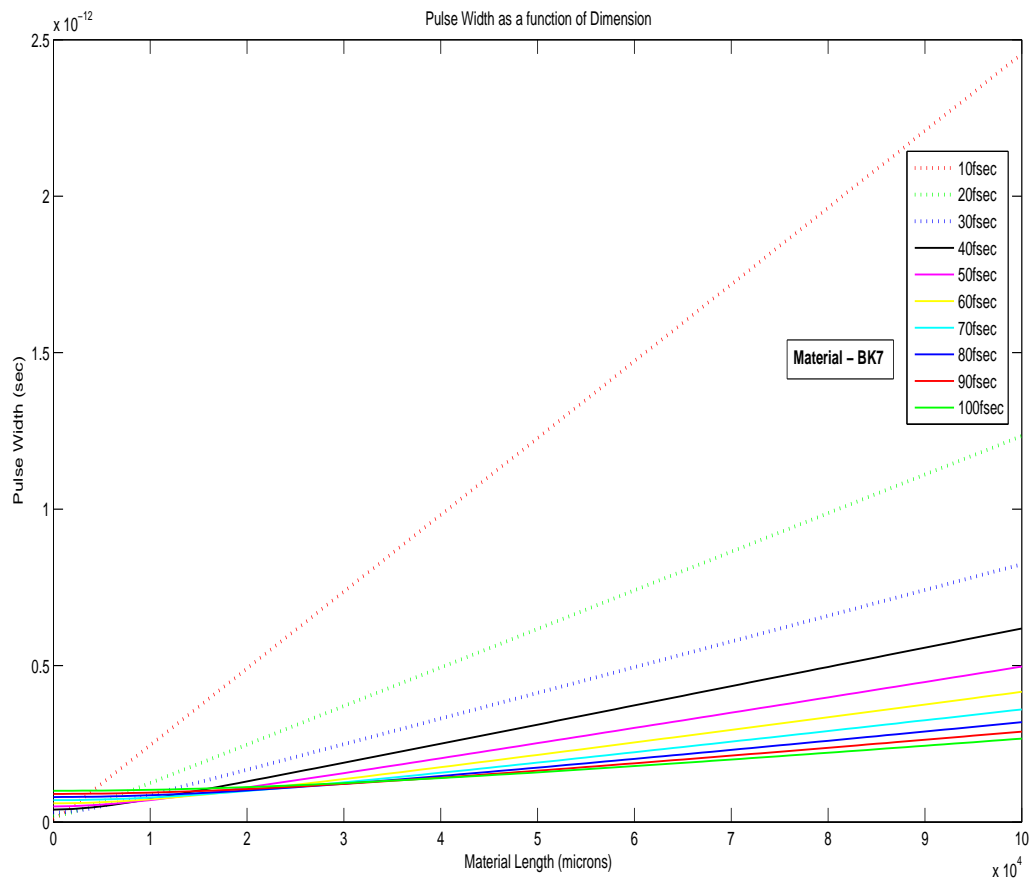
Figure 3.6 Dispersion of femtosecond pulses through BK7

3.4   Scope of Improvement

The mathematical simulation can be improved by introducing a detailed study of effects of phase changes on the pulse width. This in turn will help us understand the phase dependent pulse characteristics better. To apply the knowledge obtained from the
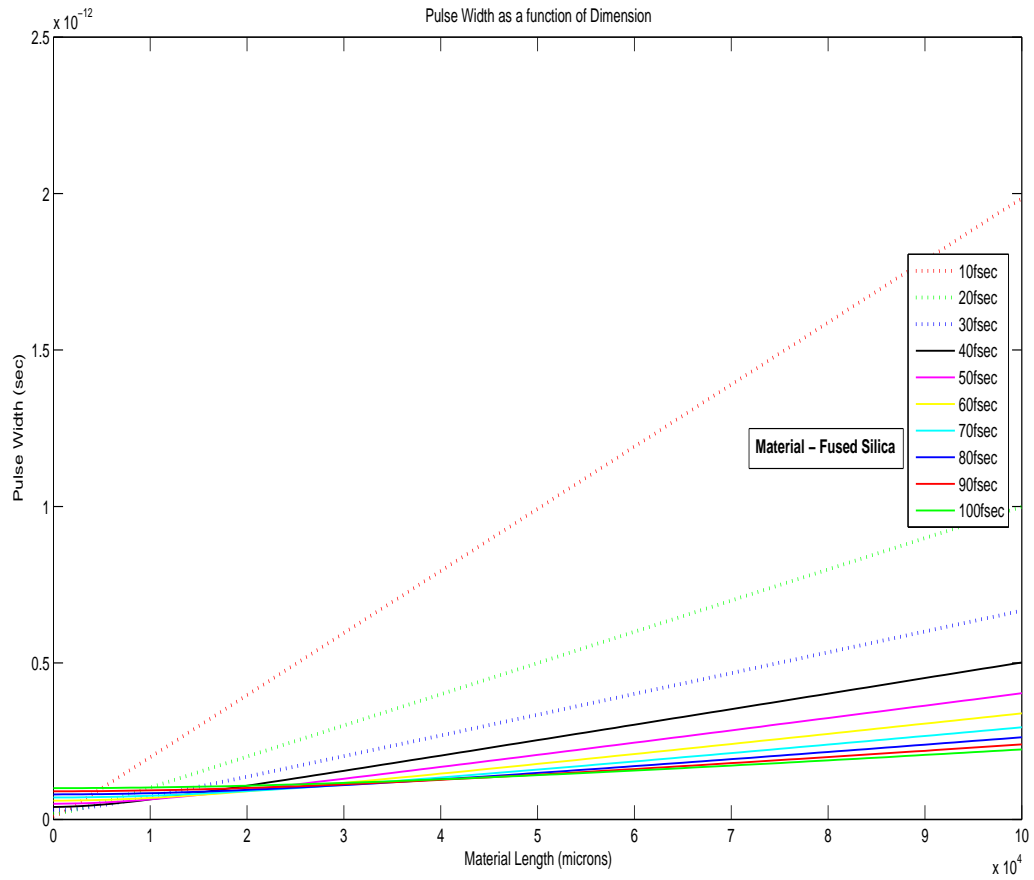
Figure 3.7 Dispersion of femtosecond pulses through Fused Silica

mathematical simulation, optical setup needs to be designed for the purpose of phase management and femtosecond pulse manipulations.
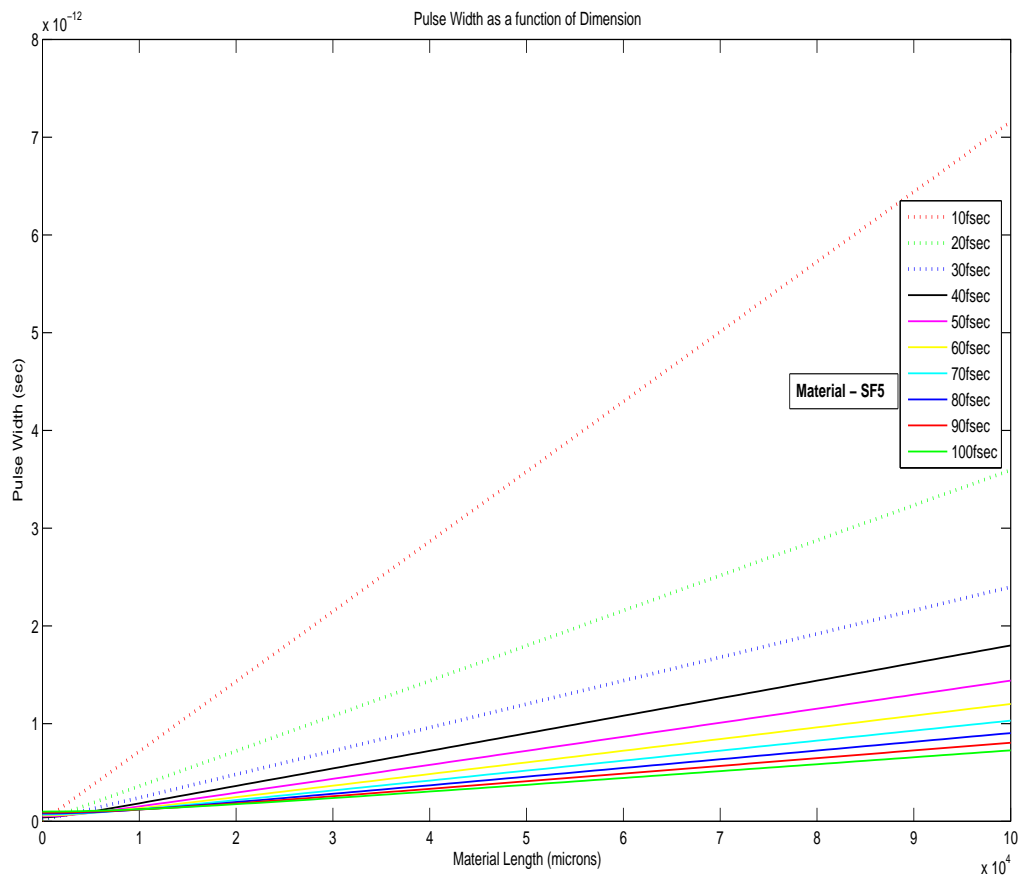
Figure 3.8 Dispersion of femtosecond pulses through SF5
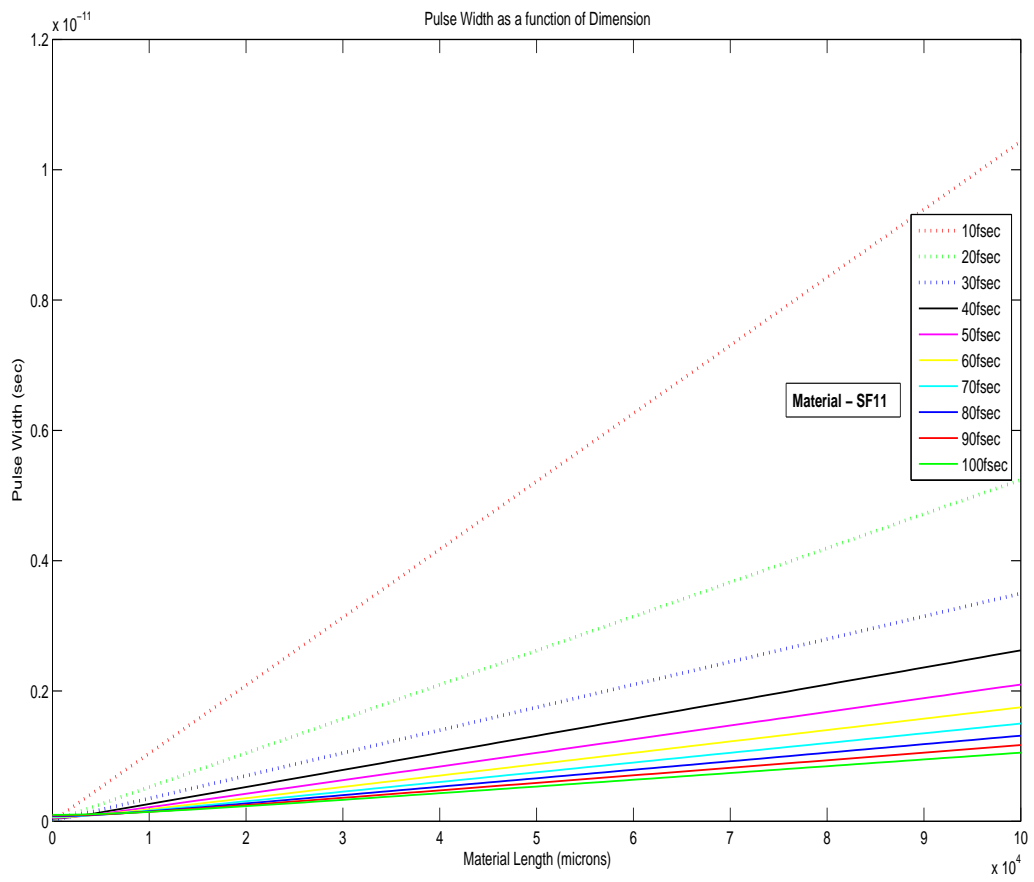
Figure 3.9 Dispersion of femtosecond pulses through SF11

CHAPTER 4

FEMTOSECOND LASER PULSE DELIVERY

The study of pulse propagation in dispersive media indicated that ultrashort pulses undergo temporal dispersion so significant that ultrashort pulses no longer remain ultrashort. The short temporal profile is the very property of the laser pulses which makes them viable for their application in multiphoton excitation fluorescence. Hence, we chose a hollow core photonic crystal fiber (PCF) for the delivery of light pulses to the multiphoton imaging system. In this chapter we will discuss the characterization of PCF.

4.1 Hollow Core Photonic Bandgap Fiber

Photonic Bandgap Fibers guide light in a hollow core, surrounded by a microstructured cladding formed by a periodic arrangement of air holed in silica. As the light is guided in the hollow core, the effects of material nonlinearities that were discussed in chapter two are significantly reduced thus providing an advantage over conventional optical fibers. The PCF that we used for our purpose was a hollow core photonic bandgap fiber $HC-800-02$ by Blaze Photonics [27]. The figure 4.1 shows the schematic diagram of a photonic crystal fiber.

4.2 Delivery setup

To focus the beam into the core of the PCF a beam expanding setup was configured. The input beam was expanded three times by using two achromatic doublet lenses in keplerian setup as show in the figure below. The focusing lens that was used to focus this expanded beam into the core ($6.8\mu m$) was an aspheric of power 10X and numerical
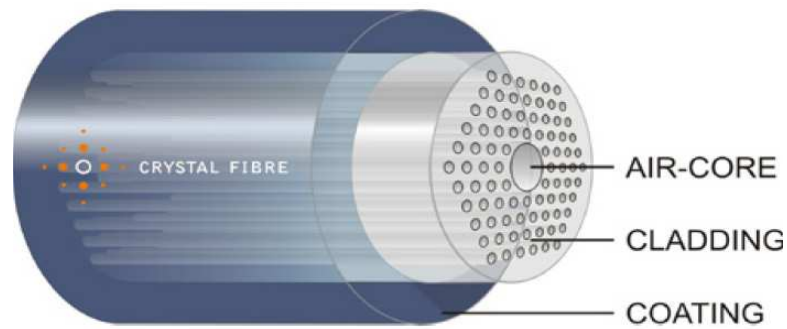
Figure 4.1 Photonic Crystal Fiber

Figure taken from http://www.crystal-fibre.com/

aperture of 0.16. Collimating optics is used at the other end of the PCF for collimating the laser beam.
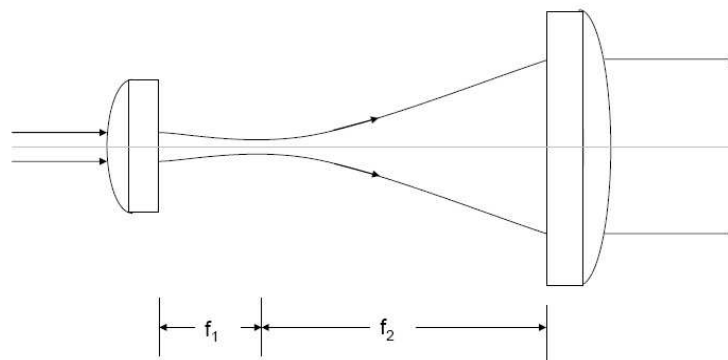
Figure 4.2 Keplerian Setup

4.3   Characterization of PCF

To characterize the PCF the following two experiments were performed:

- How input and output power change with change in the spectrum of light

- How input and output pulse width change as the spectrum of light changes

In the first experiment, the position of the prism 2 in the laser was changed to spectrum of laser light pulses. The power of laser at the focusing end and the collimating end

of the PCF was measured. Using the input and output power readings the *attenuation* of light was calculated using the following equation:

$$Attenuation = 10log_{10}\left(\frac{Outputpower}{Inputpower}\right) \tag{4.1}$$

The results obtained from this experiment are graphically represented as shown in the figure 4.3
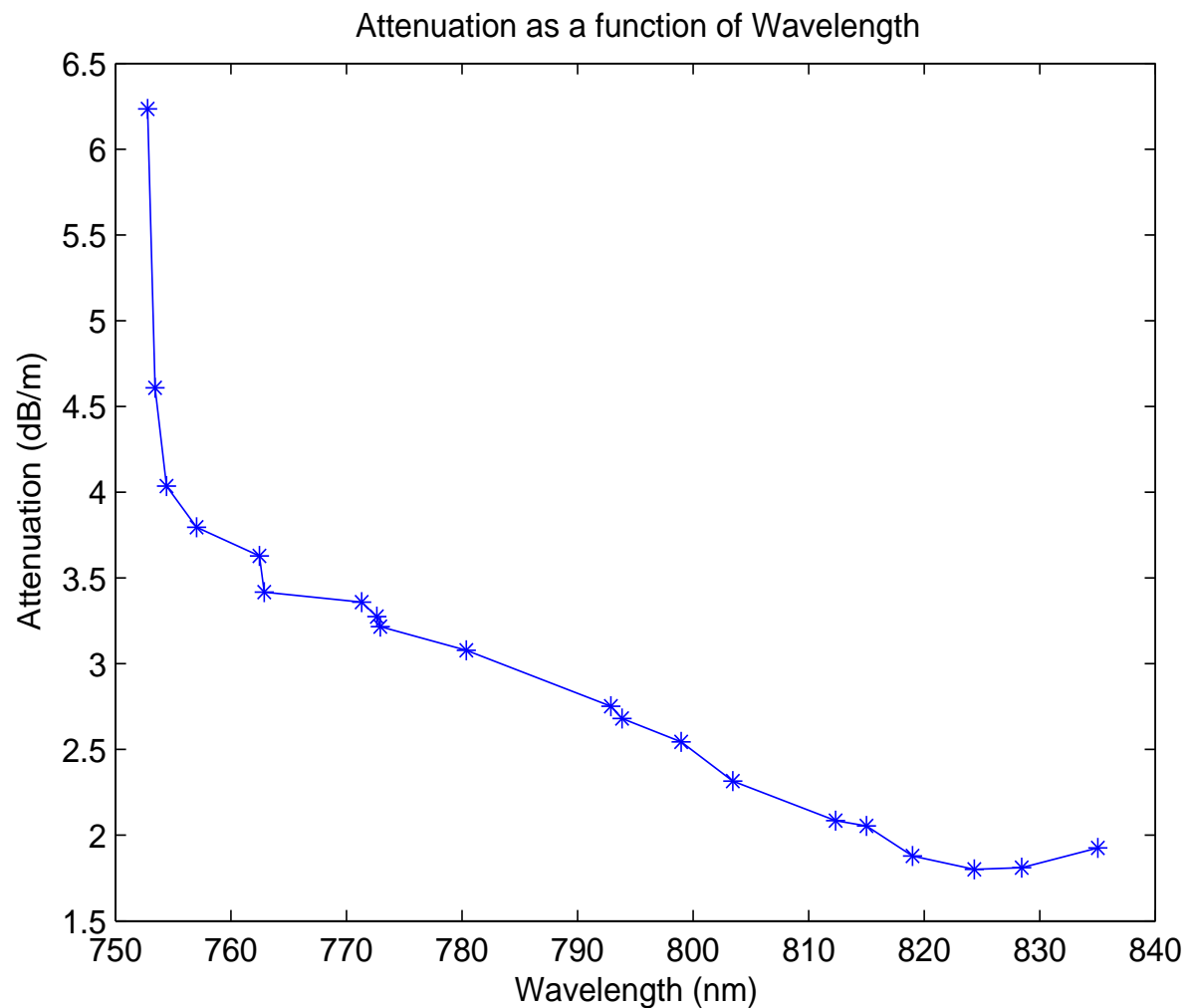
Figure 4.3 Attenuation as a function of wavelength

From this experiment it was understood that the minimum attenuation region for the PCF $HC - 800 - 02$ we were using, was between 815 nm to 835 nm figure and there was a steep increase in attenuation at wavelengths below 760 nm (figure 4.3).

In second experiment, the dispersion characteristics of the PCF were studied. The temporal profile of the input and output laser pulses were studied using the autocorrelator setup that was discussed in chapter 2. The graph (figure 4.4) shows the results that were obtained from the second experiment. From the graph the first conclusion we can draw is that using a photonic crystal fiber significantly reduces the pulse dispersion. Secondly, the input output pulsewidth difference reduces for wavelengths above $800nm$.
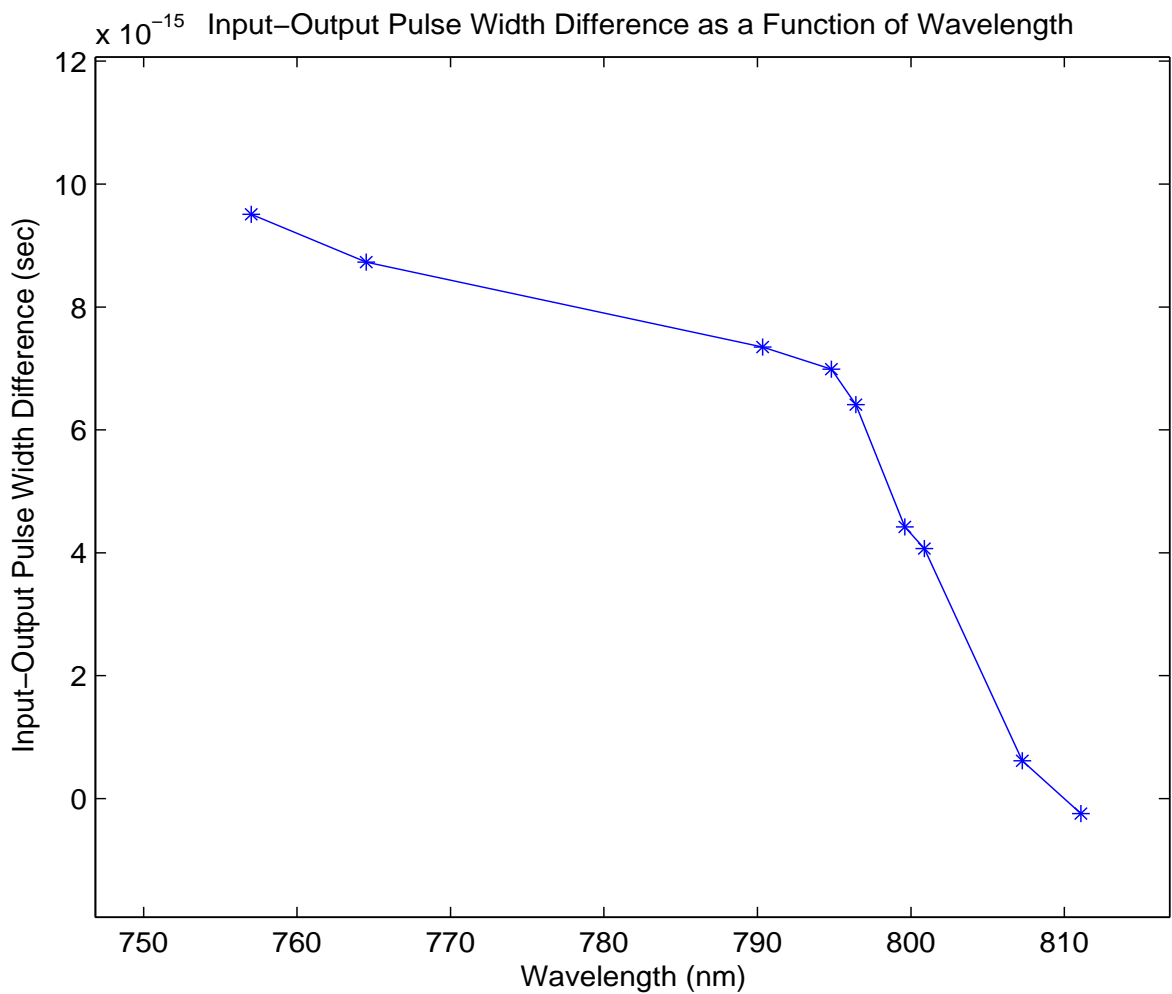
Figure 4.4 Difference in Input-Output Pulsewidth as a function of Wavelength

From the two experiments it was concluded that the fiber can be used optimally in the wavelength region between 815 nm to 840 nm.

The input and output light spectra were compared to observe any changes in the spectral content of the input and output pulse from the PCF. The results showed little or no changes.

Thus it was concluded that the photonic crystal fiber not only preserves the temporal profile of the pulse but also the spectral content of the pulse is unaltered.

CHAPTER 5

PRINCIPLE OF NON-LINEAR EXCITATION FLUORESCENCE

The constant demand of a better diagnostic imaging technique has lead to the evolution and development of an optical microscope to great limits. The resolving powers of the modern microscopes have grown powerful and unparalleled as an investigating tool of structure, function, chemistry and dynamics of molecules, proteins, nanoparticles, chromophores, fluorophores and even microbes. The modern day optical microscopes have not only overcome the diffraction limit that governed the conventional optical imaging, but also have proven to be potentially more powerful in performing sectioning deep into the tissue using contrast agents. And, non-linear excitation fluorescence microscopy is one such technique used in bio-imaging today.

This chapter provides a comprehensive review of the physics of non-linear excitation fluorescence and technical aspects of design and assembly of a multiphoton fluorescence microscope.
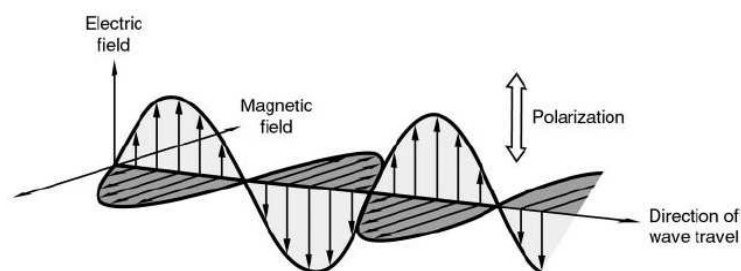
Figure 5.1 Schematic diagram of an electromagnetic wave

Figure from Biomedical Photonics Handbook, CRC Press 2003, NY USA

5.1   Light and Light Interactions

5.1.1   Light

Light is an electromagnetic radiation consisting of symbiotic oscillations of electric and magnetic fields(figure 5.1). It is that part of the electromagnetic spectrum which has wavelength range from 1000nm to 100nm. As shown in the figure 5.2, this range includes the near infrared (NIR), the visible light and the ultraviolet bands (A,B and C). This range is also called the diagnostic (or therapeutic) window and holds a great importance in the field of biomedical optical imaging.
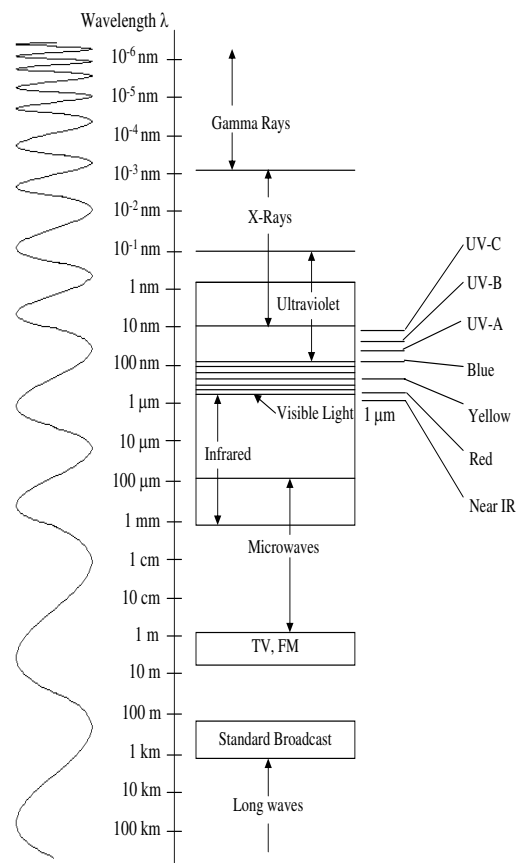
Figure 5.2 Electromagnetic Spectrum

There are two types of theories concerning light; the classical theory according to which the light is an oscillating electromagnetic field which can have a continous range

of energies (figure 5.2) and quantum theory that describes light to be made up of energy packets (quanta) called photons. The quantum theory also suggests that energy exchange between light and matter is in the form of these energy packets. The equation give below formulates the relationship between the energy of photon and the frequency of the EM wave.

$$E = h\nu = h\frac{c}{\lambda} \tag{5.1}$$

where,

E is the energy of the photon

$h = 6.6x10^{-36}Js$ is the Planck's Constant

$c = 3x10^{8}m/s$ is the speed of light in vacuum

ν and λ are the frequency and wavelength of EM wave respectively

5.1.2 Light Interactions

5.1.2.1 Bulk Interactions

The biological environment is an optically inhomogeneous media, hence there is a need to study the affect of such media on light and its propagation. There are three fundamental photophysical processes the light undergoes when it interacts with matter at bulk level.

- Refraction
- Scattering
- Absorption

Refractive index is one of the fundamental properties of a homogeneous media, which can also be defined for an inhomogeneous media. In a physical sense, refraction is the bending of the light when it travels from one media (n_1) to the other (n_2), where its speed is different from the first media (figure 5.3). Refraction of light depends on the linear optical properties of a media.

$$n = \frac{c}{c_m} \tag{5.2}$$

where,

n is refractive index

c is speed of light in vacuum

c_m speed of light in media
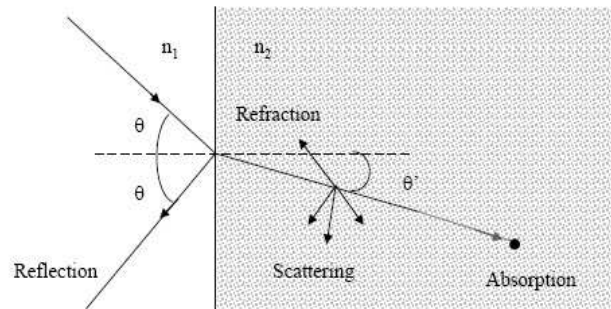
Figure 5.3 Light interaction at bulk level

Scattering occurs at localized inclusions, when the mismatch in refractive indices (n_1, n_2) occupy a focalized area in the media (figure 5.3). Scattering properties of a given media can used for diagnostic purposes as this property renders information about the size, morphology and structure of the various components in the media. Any change in the scattering properties of a biological sample can be translated into physiological information about the sample.

5.1.2.2   Molecular Level Interactions

The molecular level interaction of light holds a higher value in biomedical optical imaging compared to the bulk interaction because, these interactions have extraordinary sensitivity and selectivity. There are four ways in which light interacts at molecular level.

- Absorption
- Spontaneous Emission
- Stimulated Emission
- Raman Scattering

The interaction of light with a molecular media (nano and micro biological systems) can be described by an apporach known as *electric dipole approximation.* It is based on the electrical polarization of a molecule which is exposed to an electric field.

In the case of a linear field response, the total molecular dipole shows that the dipole moment has a linear dependance on the electric field.

$$\mu_t = -er = \mu + \alpha\epsilon(\nu')[28] \tag{5.3}$$

where,

μ_t is the total electronic dipole moment vector

e and r is the electronic charge and its position respectively

μ is the permanent dipole term in the absence of any field

$\alpha\epsilon(\nu')$ is the dipole moment induced by the electric field (μ_{in})

$\epsilon(\nu')$ is oscillating electric field of light

α is the dynamic polarizability term

μ_{in} is the polarization of the electronic cloud of the molecule under the influence of the field. This induced polarization is characterized by α, which relates the directions of the vectors; ϵ and μ_{in}.

The dipole interaction between the molecule and a radiative field $\epsilon(\nu)$ can be mathematically represented as

$$V = \epsilon(\nu)\mu + \epsilon(\nu)\alpha\epsilon(\nu')[28] \tag{5.4}$$

The first term in the equation 5.4 represents the electric field of the incident photon having frequency of ν which contributes to absorption and spontaneous and stimulated emission (figure 5.4). The second term represents Raman scattering, where the interaction of the photon with the matter causes a change in its frequency ν.
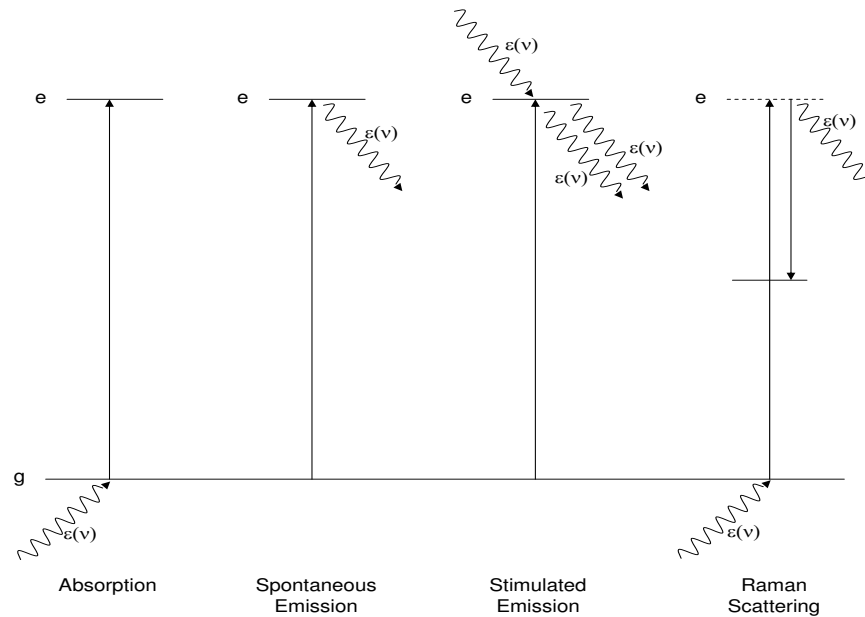
Figure 5.4 Schematics of various light-molecule interactions

Adapted from Introduction to Biophotonics, Wiley-Interscience 2003, NJ USA

5.2 Fluorescence

The phenomenon of fluorescence is a radiative photo-physical interaction of light that involves absorption and emission of energy. Now let us understand the physics of fluorescence at atomic level.

By now we know that fluorescence involves the excitation of a molecule in its ground state to higher energy level. Any electronic state (ground or excited) consists of vibrational levels. And, when the molecule absorbs the energy of the incident photon, molecule is excited from a vibrational level in the electronic ground state to one of the many vibrational levels in the electronic excited state. In most of the molecules, particularly in organic molecules electronic states can be divided into singlet states and triplet states;

- Singlet state: All electrons in the molecule are spin-paired
- Triplet state: One set of electron spins is unpaired
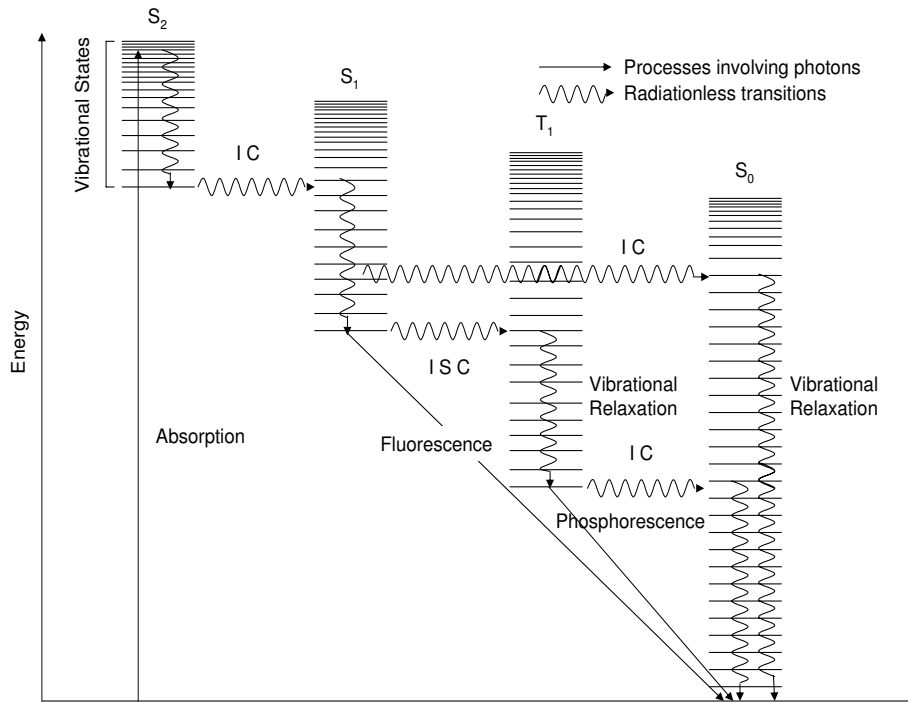
Figure 5.5 Jablonski diagram showing possible fates of excitation

Adapted from Introduction to Biophotonics, Wiley-Interscience 2003, NJ USA

The total spin in the molecules of the ground state is $S = 0$ and a spin multiplicity $2S + 1 = 1$. An exception to this is the oxygen molecule (O_2), whose ground state is a triplet with spin $S = 1$ and spin multiplicity $2S + 1 = 3$. As shown in the figure 5.5 the singlet states in the order of increasing energy from ground state are labeled S_0, S_1, S_2 so on and so forth. As shown in the figure 5.5, absorption of a photon causes the molecule to jump to a higher vibrational levels of singlet state S_2. In almost all molecule that are in a high vibrational level of the excited state will quickly fall to the lowest vibrational level of this state by losing energy to other molecules through collision. The molecule will also get rid the excess energy by means of vibration and rotation. After which the molecule undergoes a non-radiative crossing from the S_2 state to S_1 state. This crossing from one electronic state to the other of the same spin multiplicity is called *internal conversion* (IC). Whereas, when a non-radiative crossing takes place between two electronic states (S and T) with different spin multiplicity, it is called *intersystem*

crossing (ISC). Crossing to the S_1 state is followed by non radiative energy dissipation causing the molecule to fall to the lowest vibrational level in the S_1 state. At this point, the molecule can return to its electronic ground state (S_0) by emitting a photon, and this emission is known as fluorescence [28][29][30].

As the energy conversions talked about in the beginning of this section suggests that the energy of the photon absorbed is higher than the energy of the photon emitted. Since energy and the wavelength of light have inverse proportionality (equation 5.1); higher energy corresponds to shorter wavelength and lower energy corresponds to longer wavelength. Which means in the fluorescence phenomenon, excitation wavelength is shorter than the emission wavelength. Take for example Rhodamine, a common fluorophore used for staining mitochondria and staining cell line to detect apoptosis has its excitation peak at 507nm and emission peak at 529nm.

The information borne in the emitted photons in this phenomenon has a high diagnostic value. The transitions between one energy level to the other for a fluorophore is well defined at specific wavelengths serves as its spectral fingerprint. As a result fluorescence emission spectrum of a any fluorophore is specific and can be used in fluorescence diagnostics. The fluorescence spectra not only provides detail information about the fluorophore, but also about their conformity, binding sites and interaction with cells and tissues [29]. At present, various exogenous fluorescing dyes can be applied for probing cell anatomy and cell physiology [31]. Dyes such as fluorescein and indocyanine green are used for fluorescence angiography and blood volume determination.

In traditional fluorescence microscopy, fluorescence is a result of interaction of a single photon with the fluorophore. In this phenomenon the energy required for the fluorophore to be transfered to the excited state is derived from absorbing as single photon. Fluorescence microscopy has proved to have potential in imaging microbiological systems, but it has a number of disadvantages.
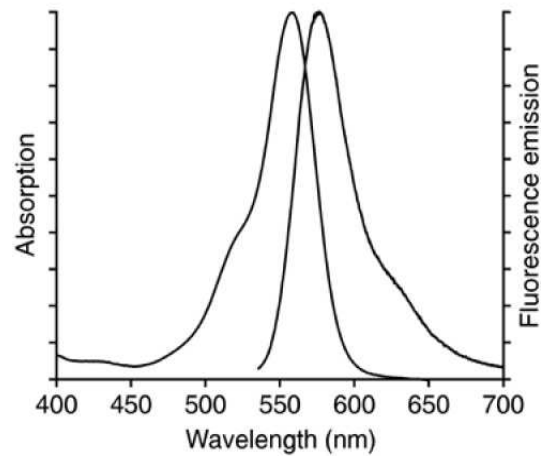
Figure 5.6 Emission and excitation spectrum of Rhodamine/pH 7.0

Invitrogen Corporation-Molecular Probes

1. Excitation spectra of most of the fluorophores used as biomedical imaging probes lie in the UV or blue-green region of the electromagnetic spectrum. And, light in this region is heavily scattered in a biological sample resulting in a low penetration depth.

2. Single-photon fluorescence is not a localized phenomenon i.e., single-photon fluorescence is not just confined to the focal point of the excitation beam. This causes the blurring of the image due to the out of focus fluorescence that is seen at the detector end. For blocking the out of focus fluorescence confocal setup can be used at the cost of amplitude of the fluorescence signal.

3. As seen in the figure 5.6 there is a considerable overlap between the excitation and emission spectra. The filtering of the excitation wavelengths at the detector results in the lose of fluorescence signal in that band.

4. Phototoxic effects of the wide-field fluorescence is a problem when imaging *in-vivo*.

5.3   Non-linear Excitation Fluorescence

Non-linear excitation of fluorescence molecules is related to the simultaneous absorption of two or more photons whose energy equals the energy for more familiar single photon excitation fluorescence [32].
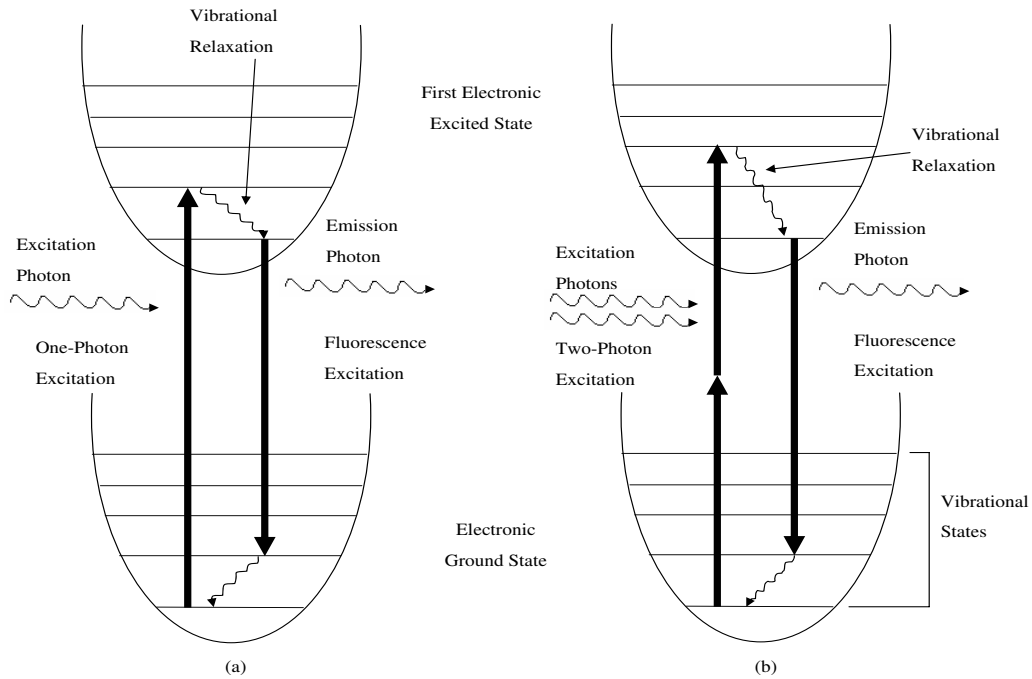
Figure 5.7 Jablonski diagram for one photon (a) and two photon (b) excitation.

Figure adapted from Biomedical Photonics Handbook, CRC Press 2003, NY USA

It was back in 1931 when Nobel Laureate G-Mayer Maria, predicted the phenomenon of two-photon absorption (non-linear absorption) in her doctoral dissertation. According to her theory, an atom or molecule could simultaneously absorb two photons in the same quantum event [33]. But the temporal window in the order of femtoseconds was a requirement for such an even to occur. It was not untill 1961, after the development of femtosecond laser sources, the detection of two-photon excitation fluorescence in CaF_2 was reported by W. Kaiser and C. B. G. Garret [34]. And, soon after in 1964 the

detection of three-photon absorption cross-section for naphthalene crystals was reported by S. Singh and L. T. Bradley [35].

As shown in the figure 5.7, in non-linear excitation the energies ($E=h\frac{c}{\lambda}$) of the two or more photons combine to excite a fluorophore to its excitation state. Let us consider the case of two-photon excitation. If two photons were to excite the fluorophore their energies E_1 and E_2 not necessarily be equal. In terms of wavelengths the necessary condition can be mathematically shown as:

$$\lambda_{1-photon} \approx \left(\frac{1}{\lambda_1} + \frac{1}{\lambda_2}\right)^{-1} \tag{5.5}$$

where, $\lambda_{1-photon}$ is the peak excitation wavelength of fluorphore for single photon excitation. And, λ_1 and λ_2 are the wavelengths of the two photons participating in exciting the fluorphore. Even if the equation 5.6 holds true, for practical reasons the experimental choice is such that [36]:

$$\lambda_1 = \lambda_2 \approx 2\lambda_{1-photon} \tag{5.6}$$

Denk and Svoboda in 1997 reported that in bright daylight the possibility of single-photon absorption to take place is about one every second and that of two-photon is one every 10 million years. Over the years great technological advancements have increased the probability of non-linear excitation of any molecule. The probability of multiphoton excitation is based on: the probability of a molecule undergoing n-photon absorption is proportional to the probability p_n of finding n photons within the volume it occupies at any moment in time [37],[38] and the probability (n_a) of finding them within the interval of time [39].

Let us try to understand the spacial probability of such occurances. Mean energy of a molecular volume (side of cube-s) when illuminated by a laser beam of wavelength λ is (assuming beam width is greater than)

$$E_m = mh\frac{c}{\lambda}[30] \tag{5.7}$$

where, m is the mean photons within a molecular volume at a given instance. The intensity (energy per unit area per unit time) of the laser beam can be shown as

$$I = \frac{E_m}{s^2 \cdot \frac{s}{c}} = \frac{mhc^2}{\lambda \cdot s^3}[30] \tag{5.8}$$

substituting $V = s^3 = $ Molar volume $= \frac{V_m}{N_a}$. Where , $N_a = 6.6023 X 10^{23} mol^{-1}$ represents avagardo's constant.

$$m = \frac{IV_m\lambda}{N_a hc^2}[30] \tag{5.9}$$

Using Poisson distribution it is found that the probability of p_n is [37]

$$p_n = \frac{m^n}{n!}e^{-m}[30],[37] \tag{5.10}$$

When the equation 5.10 is expanded using taylor series the only significant term that remains is the first term.

$$p_n = \frac{m^n}{n!}[30] \tag{5.11}$$

Substituting $n = 2$ in equation 5.11 we get

$$p_2 = \frac{m^2}{2!} \propto \gamma I^2[30] \tag{5.12}$$

The equation 5.11 suggests the quadratic dependence of two-photon excitation on the intensity of the excitation. Higher the order of non-linear excitation higher the order of dependence.

The probability of non-linear excitation also depends upon the probability of finding the photons within the interval of time. The equation below shows how the time-averaged two-photon fluorescence intensity per molecule within an arbitrary interval T is given as

$$\langle I_f(t) \rangle = \frac{1}{T}\int_0^T I_f(t)^2 dt = \delta_2 \left[\pi \frac{NA^2}{hc\lambda}\right]^2 \frac{1}{T}\int_0^T P(t)^2 dt[40],[30] \tag{5.13}$$

where,

δ_2 is molecular cross-section

$I(t)$ is the temporal characteristics of light

NA is the numerical aperture of the objective lens

$P(t)$ is the excitation power as a function of time

The equation 5.12 represents the case when the excitation is induced by continuous-wave laser for a time interval T. For a pulsed laser, the time interval $T = \frac{1}{f_p}$, where f_p is the repetition rate of the laser. For a pulsed laser the average power of the laser pulse with a pulse width of τ_p and repetition rate f_p is $\frac{P_{avg}}{\tau_p f_p}$[30]

$$\langle I_{f,p}(t)\rangle = \delta_2 \frac{P_{avg}^2}{\tau_p^2 f_p^2} \left[\pi \frac{NA^2}{hc\lambda}\right]^2 \frac{1}{T} \int_0^{\tau_p} dt = \delta_2 \frac{P_{avg}^2}{t_p f_p} \left[\pi \frac{NA^2}{hc\lambda}\right]^2 \text{[40], [30]} \qquad (5.14)$$

The probability n_a that a certain fluorophore simultaneously absorbs two photons during a single pulse in the paraxial approximation is given by [3],

$$n_a \propto \delta_2 \frac{P_{avg}^2}{\tau_p f_p} \left(\frac{NA^2}{2\eta c\lambda}\right)^2 \qquad (5.15)$$

where, $\eta = \frac{h}{2\pi}$

P_{avg} is the time averaged power of the beam

λ is the excitation wavelength

The equation 5.7 to equation 5.15 mathematically validate the following:

- The probability (p_2) of TPE has a quadratic dependence on the Intensity (I) of excitation.

- The shorter the temporal pulse width (τ_p) of the excitation the higher the probability of TPE (n_a)

- The higher the repetition rate (f_p) of pulses the higher the probability of excitation (n_a)

- The probability of TPE can be increased by increasing the NA of the objective lens used to focus the beam on to the sample

- The probability (n_a) of TPE has a quadratic dependence on time averaged power of the incident beam

All the above parameters can be used as controlled variables for getting desired non-linear excitation of the sample.

Advantages of Non-linear Excitation Fluorescence:

1. In non-linear excitation fluorescence the excitation wavelengths are longer than the emission wavelengths. An important advantage of MPE is that the excitation wavelengths lie in the near infra-red (NIR) region of the electromagnetic spectrum. NIR is that part of the EM spectrum suffers less scattering in biological tissues resulting in higher penetration depths.

2. Non-linear excitation is a highly localized phenomenon observed at the focus of the excitation beam which prevents from imaging out of focus fluorescence to be imaged, increasing the signal to background ratio. Since all the photons emitted can be used for generating an image, no confocal blocking apertures or descanning optics are needed.

3. In non-linear excitation fluorescence phenomenon the incident photons excites fluorophores only at the focal plain considerably reduces the photo generation of toxic products.

4. The excitation and the emission spectra far away from each other in EM spectrum, thus filtering of the excitation wavelengths does not cost the fluorescence signal.

5. Since fluorescence signal has a non-linear dependence on the intensity of the incident excitation beam. Any small change in intensity of the incident beam can enhance the fluorescence signal to a higher level.

6. The most important attribute of non-linear excitation fluorescence is its inherent 3D sectioning capability which due to its quadratic and higher order dependence.

5.4   Design and Architecture of MPM

The final step of the thesis was to design and build an experimental setup for a multiphoton microscope to biological imaging. In this section we will the discuss the design aspects to optimize the two-photon signals. The design of the MPM system is as shown in the figure 5.8.

Beam
Expanding
Setup

1

2

3

4

5

6

7

8

Photomultiplier
Tube

1,7 – PCF in Fiber Mount

2 – Collimating Lens in a tube

3 – Dichoric

4 – Cage Cube

5 – High NA Aspherical Lens

6 – Focusing Lens

8 – Fluorescent Sample
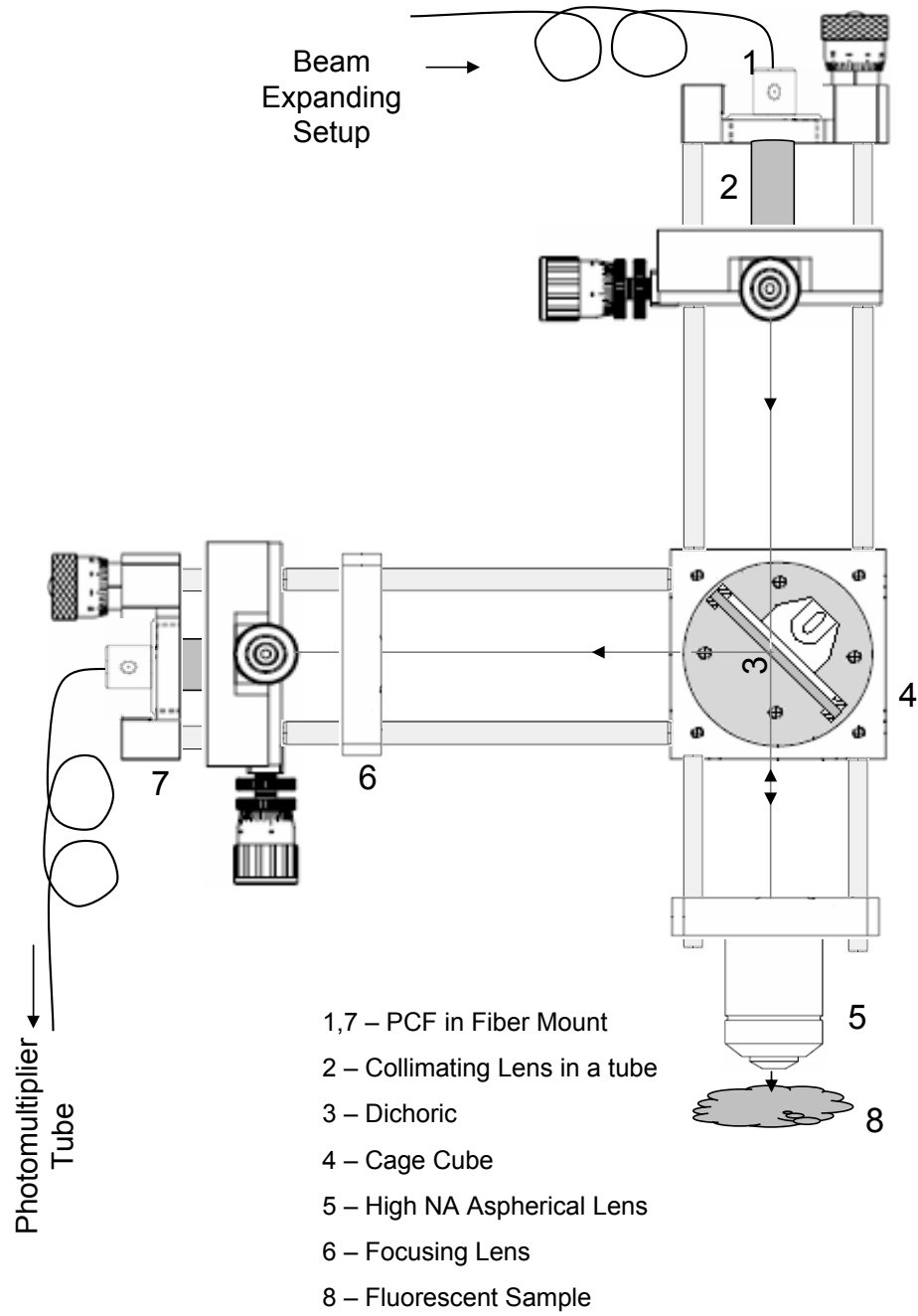
Figure 5.8 Multiphoton setup

5.4.1 Excitation Source

The MPM system consists of a 5W Coherent Verdi green laser that pumps the Ti:Sapphire laser which is used as the source of excitation for the MPM system. The laser has a wavelength tunability between $700 - 900$ nm. Using the 5W Verdi laser pump source, the output power of the Ti:Sapphire laser that can be attained is ≈ 500 mW. The output power of the laser can be controlled using neutral density filters in the path of the laser beam. For the generation of ultrashort pulses the laser is mode locked and for MPM application the laser is used at a center wavelength of 820 nm.

5.4.2 Dichoric

A long wavelength pass dichroic beam-splitter (Semrock FF665-Di01-25x36) [41] is placed in the two-photon pathway just before the objective. This filter allow the excitation light ($\lambda > 680$ nm) to pass to the objective lens, which focuses the light on to the sample. The reflection bands of this dichoric beam-splitter are in the range $350 - 650$ nm, i.e., it reflects the fluorescence signal that is picked up from the sample on to the fiber that carries the signal to the detection system. The transmission and the reflectance wavelengths of dichoic beam-splitter used are as shown in the figure 5.9.

5.4.3 Detection system

The detection system consists of a large core multimode fiber that guides the fluorescence signal to the photomultiplier tube (Hamamatsu Corp.). The detector is a H5784 series photosensor module comprising of a metal packaged photomultiplier tube, a low-power consumption high-voltage power supply and a low noise amplifier. The electric current output of the PMT is converted in to a voltage output by an amplifier. The current to voltage conversion factor of the module is 1 $V/\mu A$. The spectral response of the module is from 300 to 600 nm.
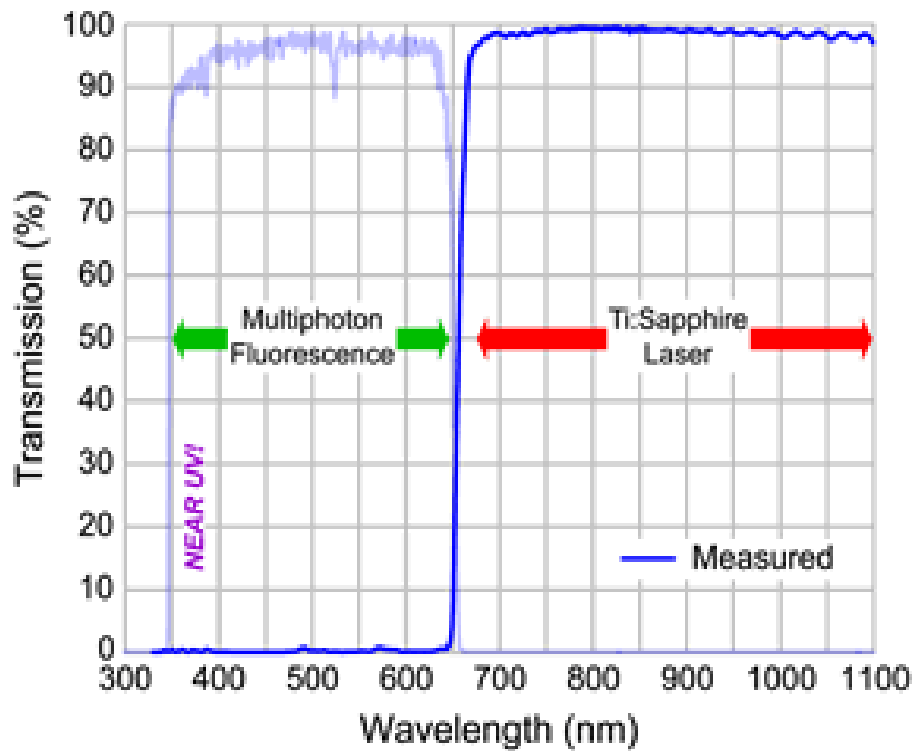
Figure 5.9 Dichroic Beamsplitter Transmission and Reflectance Curve

Graph taken from http://www.semrock.com

5.5   Scope of Improvement

Swaping the excitation source arm and the detection arm of the setup and using a short pass dichroic is another MPM setup design that can be used. An higher NA objective lens will highly increase the non-linear excitation of the molecules increasing the multiphoton signal. The PMT used is a photosensor module with gives an analog voltage output proportional to the detected multiphoton fluorescence. For detection of low fluorescence levels, using an single photon counting modules are much effective.

This thesis work started with the vision of a comprehensive multiphoton microscopy system that can be used not only for biological imaging but also for nano-surgeries, tissue ablation and other laser applications. This MPM system was to have the following key features:

1. Pulse diagnosis setup
2. Pulse manipulation setup
3. Flexible delivery of light pulses
4. Beam steering setup
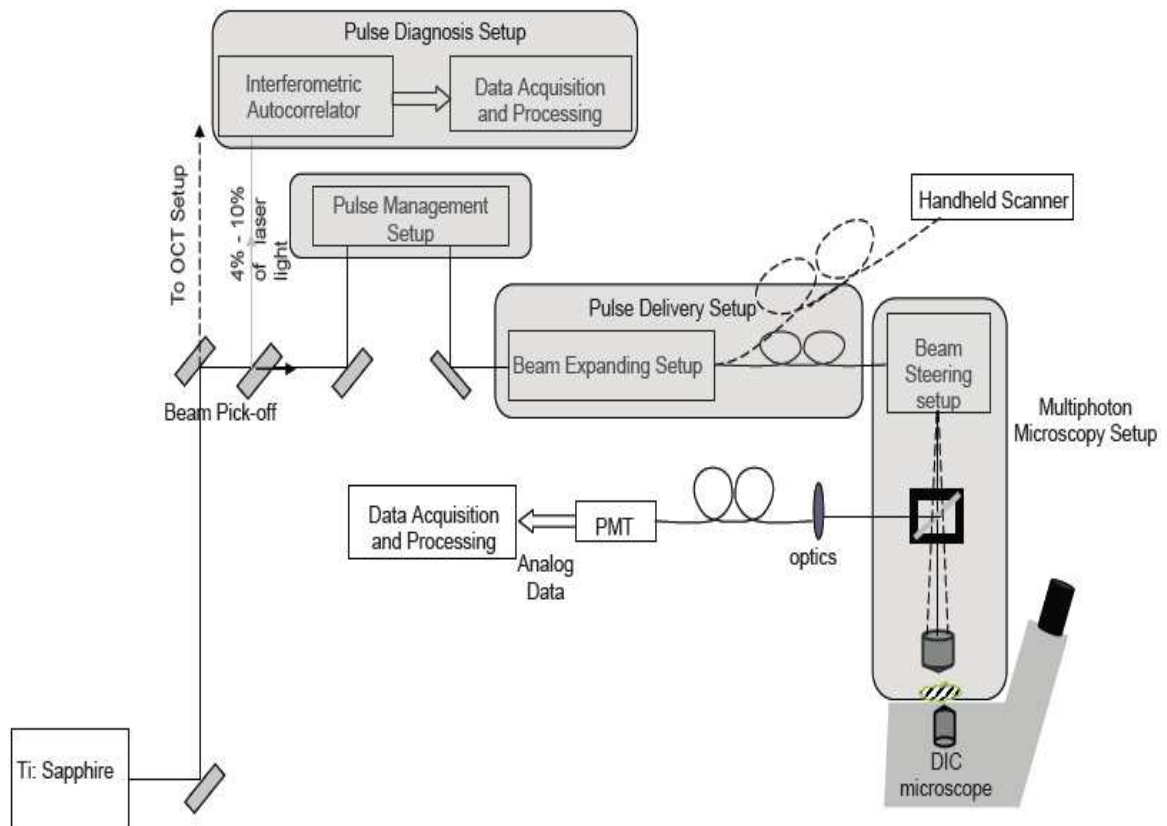
Figure 6.1 Block diagram of Multiphoton Microscopy System

6.1   Future Work

This thesis work involved working on the first three key features of the MPM system. Also, an experimental MPM setup was built as discussed in chapter 5, but it lacked a scanning or a beam steering setup. The future work involves the completion of the vision of the MPM system.
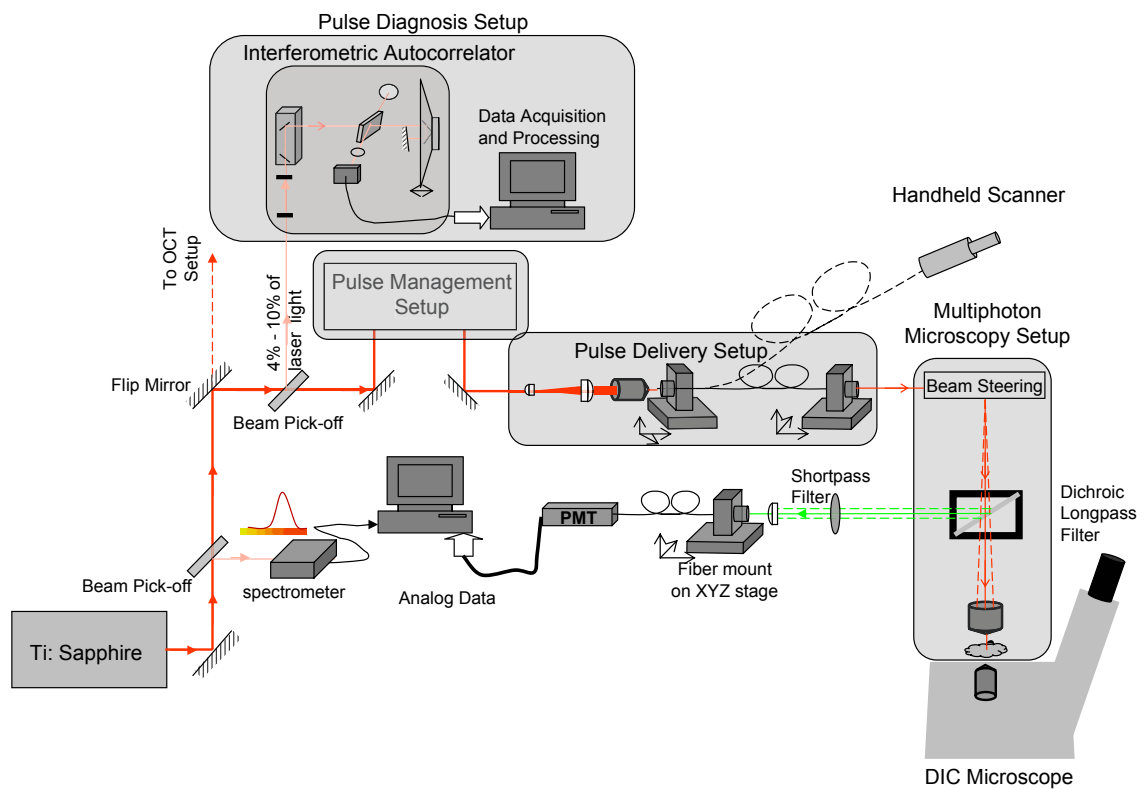
Figure 6.2 Detailed diagram of Multiphoton Microscopy System

The following are the requirements for completion of the MPM system:

1. Software controlled beam steering setup capable of xy-scanning of the biological sample.

2. Photomultiplier tube calibration

3. Interfacing photomultiplier tube with computer

4. System calibration and optimization
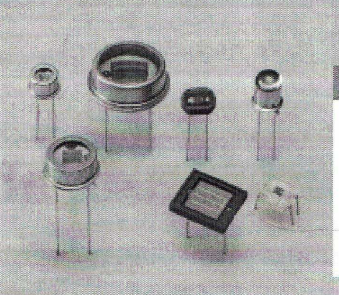
5. Integration of the MPM setup with OCT and DIC microscope

APPENDIX A

DATASHEETS

PHOTODIODE

GaAsP photodiode
Diffusion type

Photodiode for visible light detection

Features
- Low dark current
- High stability

Applications
- Analytical instrument
- Color identification

■ General ratings / Absolute maximum ratings

Type No.	Dimensional outline/ Window material *	Package	Active area size (mm)	Effective active area (mm²)	Absolute maximum ratings		
					Reverse voltage V_R Max. (V)	Operating temperature Topr (°C)	Storage temperature Tstg (°C)
G1115	①/K	TO-18	1.3 × 1.3	1.66	5	-30 to +80	-40 to +85
G1116	②/K	TO-5	2.7 × 2.7	7.26			
G1117	③/K	TO-8	5.6 × 5.6	29.3			
G1118	④/R	Ceramic	1.3 × 1.3	1.66			
G1120	⑤/R	Ceramic	5.6 × 5.6	29.3			
G3067	⑥/L	TO-18	1.3 × 1.3	1.66			
G2711-01	⑦/R	Plastic	1.3 × 1.3	1.66			

■ Electrical and optical characteristics (Typ. Ta=25 °C, unless otherwise noted)

Type No.	Spectral response range λ (nm)	Peak sensitivity wavelength λp (nm)	Photo sensitivity S (A/W)			Short circuit current Isc 100 k		Dark current ID Max.		Temp. coefficient of ID TCID (times/°C)	Rise time tr V_R=0 V R_L=1 kΩ (µs)	Terminal capacitance Ct V_R=0 V f=10 kHz (pF)	Shunt resistance Rsh V_R=10 mV		NEP (W/Hz$^{1/2}$)
			λp	GaP LED 560 nm	He-Ne laser 633 nm	Min. (µA)	Typ. (µA)	V_R=10 mV (pA)	V_R=1 V (pA)				Min. (GΩ)	Typ. (GΩ)	
G1115	300 to 680	640	0.3	0.29	0.29	0.12	0.15	1	10	1.07	1	300	10	80	1.5 × 10⁻¹⁵
G1116						0.45	0.6	2.5	25		4	1400	4	30	2.5 × 10⁻¹⁵
G1117						2	2.5	5	50		15	6000	2	15	3.5 × 10⁻¹⁵
G1118						0.12	0.15	1	10		1	300	10	80	1.5 × 10⁻¹⁵
G1120						2	2.5	5	50		15	6000	2	15	3.5 × 10⁻¹⁵
G3067						0.75	0.95	1	10		1	300	10	80	1.5 × 10⁻¹⁵
G2711-01						0.15	0.18	1	10		1	300	10	80	1.5 × 10⁻¹⁵

* Window material K: borosilicate glass, L: lens type borosilicate glass, R: resin coating

SOLID STATE DIVISION

HAMAMATSU

Figure A.1 Datasheet of GaAsP 1116

■ Spectral response

KGPDB0019EA

■ Photo sensitivity temperature characteristic

KGPDB0020EA
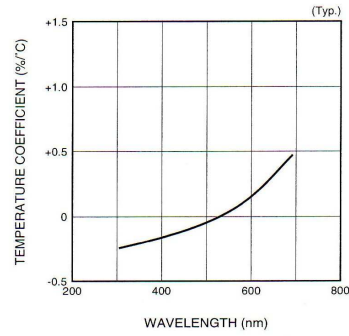
■ Rise time vs. load resistance

KGPDB0021EA
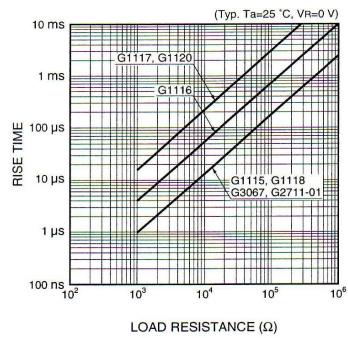
■ Dark current vs. reverse voltage

KGPDB0022EA
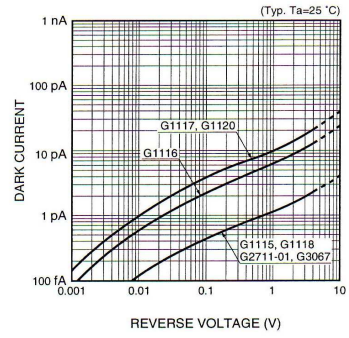
■ Shunt resistance vs. ambient temperature

KGPDB0023EA
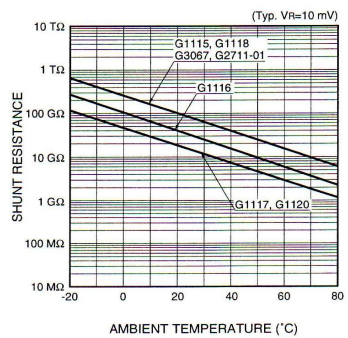
■ Short circuit current linearity

KGPDB0008EA

Figure A.2 Datasheet of GaAsP 1116 contd.

SPECIFICATIONS

ELECTRICAL

At $V_{CC} = \pm15VDC$ and $T_A = +25°C$, unless otherwise noted.

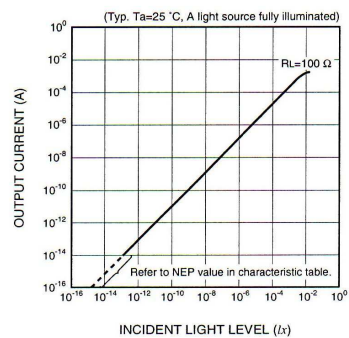| PARAMETER	CONDITION	OPA124U, P MIN	OPA124U, P TYP	OPA124U, P MAX	OPA124UA, PA MIN	OPA124UA, PA TYP	OPA124UA, PA MAX	OPA124PB MIN	OPA124PB TYP	OPA124PB MAX	UNITS
INPUT NOISE											
Voltage, $f_O = 10Hz$[4]			40	80		*	*		*	*	$nV/\sqrt{Hz}$
$f_O = 100Hz$[4]			15	40		*	*		*	*	$nV/\sqrt{Hz}$
$f_O = 1kHz$[4]			8	15		*	*		*	*	$nV/\sqrt{Hz}$
$f_O = 10kHz$[5]			6	8		*	*		*	*	$nV/\sqrt{Hz}$
$f_B = 10Hz$ to $10kHz$[5]			0.7	1.2		*	*		*	*	$\mu Vrms$
$f_B = 0.1Hz$ to $10Hz$			1.6	3.3		*	*		*	*	μVp-p
Current, $f_B = 0.1Hz$ to $10Hz$			9.5	15		*	*		*	*	fAp-p
$f_O = 0.1Hz$ thru $20kHz$			0.5	0.8		*	*		*	*	$fA/\sqrt{Hz}$
OFFSET VOLTAGE[1]											
Input Offset Voltage	$V_{CM} = 0VDC$		±200	±800		±150	±500		±100	±250	μV
vs Temperature	$T_A = T_{MIN}$ to T_{MAX}		±4	±7.5		±2	±4		±1	±2	$\mu V/°C$
Supply Rejection	$V_{CC} = \pm10V$ to $\pm18V$	88	110		90	*		100	*		dB
vs Temperature	$T_A = T_{MIN}$ to T_{MAX}	84	100		86	*		90	*		dB
BIAS CURRENT[1]											
Input Bias Current	$V_{CM} = 0VDC$		±1	±5		±0.5	±2		±0.35	±1	pA
OFFSET CURRENT[1]											
Input Offset Current	$V_{CM} = 0VDC$		±1	±5		±0.5	±1		±0.25	±0.5	pA
IMPEDANCE											
Differential			$10^{13} \| 1$			*			*		$\Omega \| pF$
Common-Mode			$10^{14} \| 3$			*			*		$\Omega \| pF$
VOLTAGE RANGE											
Common-Mode Input Range		±10	±11		*	*		*	*		V
Common-Mode Rejection	$V_{IN} = \pm10VDC$	92	110		94	*		100	*		dB
vs Temperature	$T_A = T_{MIN}$ to T_{MAX}	86	100		*	*		90	*		dB
OPEN-LOOP GAIN, DC											
Open-Loop Voltage Gain	$R_L \geq 2k\Omega$	106	125		*	*		120	*		dB
FREQUENCY RESPONSE											
Unity Gain, Small Signal			1.5			*			*		MHz
Full Power Response	$20Vp$-p, $R_L = 2k\Omega$	16	32		*	*		*	*		kHz
Slew Rate	$V_O = \pm10V$, $R_L = 2k\Omega$	1	1.6		*	*		*	*		V/μs
THD			0.0003			*			*		%
Settling Time, 0.1%	Gain = −1, $R_L = 2k\Omega$		6			*			*		μs
0.01%	10V Step		10			*			*		μs
Overload Recovery,											
50% Overdrive[2]	Gain = −1		5			*			*		μs
RATED OUTPUT											
Voltage Output	$R_L = 2k\Omega$	±11	±12		*	*		*	*		V
Current Output	$V_O = \pm10VDC$	±5.5	±10		*	*		*	*		mA
Output Resistance	DC, Open Loop		100			*			*		Ω
Load Capacitance Stability	Gain = +1		1000			*			*		pF
Short Circuit Current		10	40		*	*		*	*		mA
POWER SUPPLY											
Rated Voltage			±15			*			*		VDC
Voltage Range, Derated		±5		±18	*		*	*		*	VDC
Current, Quiescent	$I_O = 0mADC$		2.5	3.5		*	*		*	*	mA
TEMPERATURE RANGE											
Specification	T_{MIN} and T_{MAX}	−25		+85	*		*	*		*	°C
Storage		−65		+125	*		*	*		*	°C
θ Junction-Ambient: PDIP			90			*			*		°C/W
SOIC			100			*			*		°C/W

* Specification same as OPA124U, P

NOTES: (1) Offset voltage, offset current, and bias current are measured with the units fully warmed up. For performance at other temperatures see Typical Performance Curves. (2) Overload recovery is defined as the time required for the output to return from saturation to linear operation following the removal of a 50% input overdrive. (3) For performance at other temperatures see Typical Performance Curves. (4) Sample tested, 98% confidence. (5) Guaranteed by design.

Figure A.3 Specification sheet of OPAMP OPA124

blazephotonics
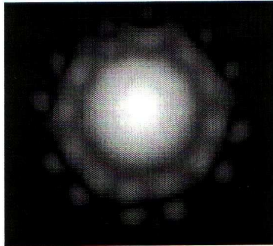
Measured near field intensity
(Log, 20 dB range)

Optical properties	
• Center operating wavelength	840 nm
• Attenuation at center operating wavelength	< 250 dB/km
• Dispersion at center operating wavelength	200 ps/nm/km
• Dispersion slope:	
- at operating wavelength	0.1 ps/nm^2/km
- at zero dispersion wavelength	15.3 ps/nm^2/km
• Width of transmission band[1]	> 90 nm
• Mode field diameter[2]	5.0 μm
• Effective mode index	~0.99

Physical properties	
• Core diameter[3]	6.8 μm
• Pitch (distance between cladding hole centers)	2.2 μm
• Air Filling Fraction in the holey region[4]	> 90%
• Diameter of holey region	41μm
• Diameter of silica cladding	130 μm
• Coating diameter (single layer acrylate)	220 μm
• Available length	up to 20 m

Figure A.4 Optical and physical properties of PCF

Semrock.

Home   Catalog Products   OEM Capabilities   About Us   News & Events   Careers   Contact Us

BrightLine® Multiphoton Fluorescence Filters
Common Specifications

Common specifications for Multiphoton sets: All BrightLine fluorescence filters adhere to a rigorously defined set of specifications to ensure consistent high performance.

| Property	Emitter	Dichroic	Comments
Guaranteed Transmission	> 90%	> 90%	Averaged over any 50 nm (emitter) or 10 nm (dichroic) window
Typical Transmission	> 95%	> 95%	within the passband
Dichroic Reflection	N/A	> 98%	Averaged over any 30 nm window within the reflection band
Angle of Incidence	0° ± 5°	45° ± 1.5°	Range of angles over which optical specs are guaranteed for collimated light
Cone Half Angle [1]	7°	2°	For uniformly distributed non-collimated light
Autofluorescence	Ultra-low	Ultra-low	Fused silica substrate
Transverse Dimensions	25.0 mm	25.2 x 35.6 mm	
Transverse Tolerance	+ 0.0 / − 0.1 mm	± 0.1 mm	
Clear Aperture	> 22 mm	> 80%	Area over which all optical specs are met
Thickness	3.5 mm	1.05 mm	
Thickness Tolerance	± 0.1 mm	± 0.05 mm	
Edge Chipping	N/A	< 0.1 mm	Measured from substrate edge
Ring Housing Material	Aluminum, black-anodized	N/A	Exciter and emitter only
Surface Quality	60-40 scratch-dig		As per MIL-C-48497A
Transmitted Wavefront Error	< λ / 4 RMS at λ = 633 nm		Peak-to-valley error < 5 x RMS
Coating Type	"Hard" ion-beam-sputtered		
Blocking	Emitter filters have exceptional blocking over the Ti:Sapphire laser range as needed to achieve superb signal-to-noise ratios even when using an extended-response PMT or a CCD camera or other silicon-based detector; detailed specifications on the main Multiphoton filter page.		
Pulse Dispersion	Dichroic beamsplitters are suitable for use with 100 femtosecond gaussian laser pulses.		
Reliability and Durability	Ion-beam-sputtered, hard-coated technology with epoxy-free, single-substrate construction for unrivaled filter life. BrightLine filters are rigorously tested and proven to MIL-STD-810F and MIL-C-48497A environmental standards.		
Emitter Orientation	The emitter orientation does not affect its performance; therefore there is no arrow on the ring to denote a preferred orientation.		
Dichroic Orientation	"Reflective coating side" should face toward detector and sample; *see diagrams below.*		
Microscope Compatibility	These filters fit most standard-sized microscope cubes from Nikon, Olympus, and Zeiss and may also be mounted in optical-bench mounts. Contact us for special filter sizes.		

[1] Filter performance is likely to remain satisfactory for Cone Half Angles as large as 10° for exciters and emitters, and 3° for dichroics.

Figure A.5 Specification sheet of dichroic

Metal package PMT
Photosensor Modules H5784 Series
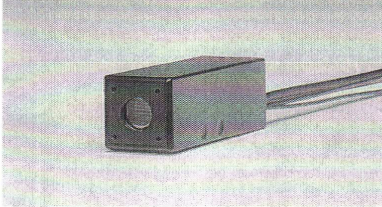
The H5784 series photosensor modules are comprised of a metal package photomultiplier tube, a low-power consumption high-voltage power supply and a low noise amplifier. The electrical current from the photomultiplier tube is converted to a voltage by an amplifier for easy signal processing. The H5784 is highly resistant to noise since the amplifier is installed near the anode output pin of the photomultiplier tube. The amplifier feedback resistance of 1 MΩ allows a current-to-voltage conversion factor of 1 V/μA, and covers a frequency bandwidth from DC to 20 kHz.

Product Variations

Type No.	Spectral Response	Current-to-voltage Conversion Factor	Frequency Bandwidth	Features
H5784	300 nm to 650 nm			For general applications in visible range
H5784-01	300 nm to 850 nm			For general applications in visible to near IR range
H5784-02	300 nm to 880 nm			High sensitivity in near IR range.
H5784-03	185 nm to 650 nm	1 V/μA	DC to 20 kHz	For UV to visible range
H5784-04	185 nm to 850 nm			For UV to near IR range
H5784-06	185 nm to 650 nm			For UV to visible range (synthetic silica window) with higher sensitivity below 300 nm than -03 type
H5784-20	300 nm to 900 nm			Infrared-extended multialkali photocathode with enhanced sensitivity

Specifications

Parameter		H5784 Series				Unit
Suffix		None/-03/-06	-01/-04	-02	-20	—
Input Voltage		±11.5 to ±15.5				V
Max. Input Voltage		±18				V
Max. Input Current		+9/-1				mA
Max. Output Signal Voltage		+10 (load resistance 10 kΩ)				V
Max. Control Voltage		+1.0 (Input impedance 100 kΩ)				V
Recommended Control Voltage Adjustment Range		+0.25 to +0.9				V
Effective Area		ϕ8				mm
Sensitivity Adjustment Range		1: 10^4				—
Peak Sensitivity Wavelength		420	400	500	630	nm
Cathode — Luminous Sensitivity	Min.	40	80	200	350	μA/lm
	Typ.	70	150	250	500	
Cathode — Blue Sensitivity Index (CS 5-58)		8	—	—	—	—
Cathode — Red/White Ratio		—	0.2	0.25	0.45	—
Cathode — Radiant Sensitivity *1		62	60	58	78	mA/W
Anode — Luminous Sensitivity *2	Min.	1.0×10^7	1.5×10^7	2.5×10^7	3.5×10^7	V/lm
	Typ.	5.0×10^7	7.5×10^7	1.25×10^8	2.5×10^8	
Anode — Radiant Sensitivity *1 *2		43	30	29	39	V/nW
Anode — Voltage Output Depending on PMT Dark Current *2 *3	Typ.	0.2	0.4	2	2	mV
	Max.	2	4	20	20	
Current-to-Voltage Conversion Factor		1				V/μA
Offset Voltage *2	Typ.	±3				mV
Ripple Noise *2 *4 (peak to peak)	Max.	2				mV
Settling Time *5		2				s
Operating Ambient Temperature		+5 to +50				°C
Storage Temperature		-20 to +50				°C
Weight		100				g

*1: Measured at the peak sensitivity wavelength   *2: Control voltage = +0.8 V   *3: After 30 minute storage in darkness
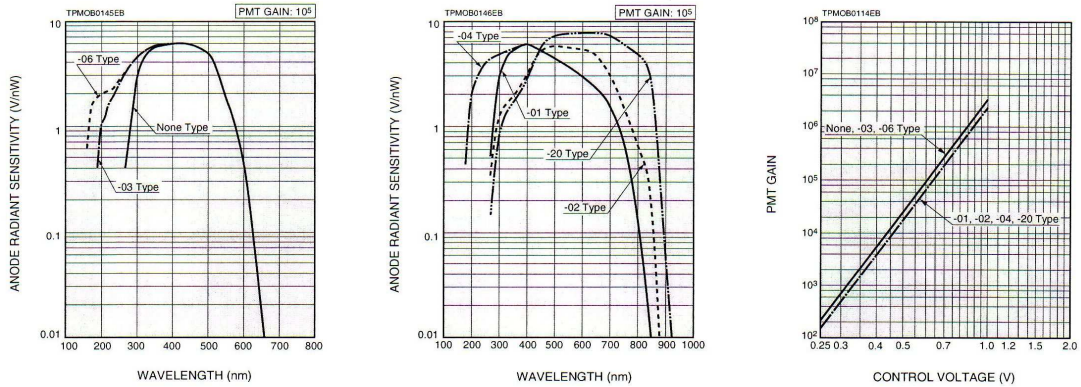*4: Cable RG-174/U, Cable length 450 mm, Load resistance = 1 MΩ, Load capacitance = 22 pF
*5: The time required for the output to reach a stable level following a change in the control voltage from +1.0 V to +0.5 V.
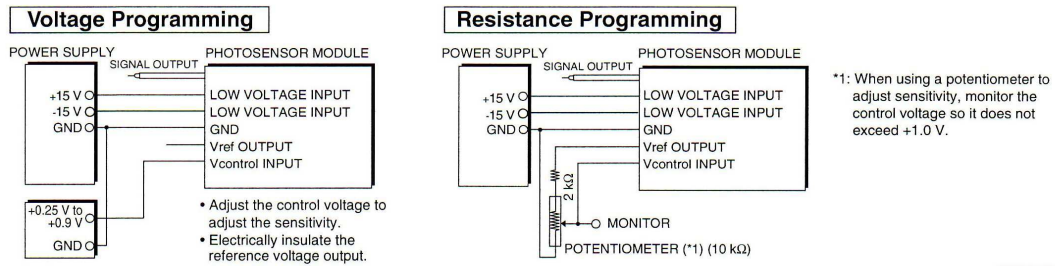
Figure A.6 Specification sheet of PMT

Voltage Output Type Photosensor Modules

Characteristics (Anode radiant sensitivity, PMT gain)

TPMOB0145EB PMT GAIN: 10^5

-06 Type
None Type
-03 Type

ANODE RADIANT SENSITIVITY (V/nW)
WAVELENGTH (nm)

TPMOB0146EB PMT GAIN: 10^5

-04 Type
-01 Type
-20 Type
-02 Type

ANODE RADIANT SENSITIVITY (V/nW)
WAVELENGTH (nm)

TPMOB0114EB

None, -03, -06 Type
-01, -02, -04, -20 Type

PMT GAIN
CONTROL VOLTAGE (V)

Sensitivity Adjustment Method

Voltage Programming

POWER SUPPLY
SIGNAL OUTPUT
PHOTOSENSOR MODULE

+15 V
-15 V
GND

LOW VOLTAGE INPUT
LOW VOLTAGE INPUT
GND
Vref OUTPUT
Vcontrol INPUT

+0.25 V to +0.9 V
GND

• Adjust the control voltage to adjust the sensitivity.
• Electrically insulate the reference voltage output.

Resistance Programming

POWER SUPPLY
SIGNAL OUTPUT
PHOTOSENSOR MODULE

+15 V
-15 V
GND

LOW VOLTAGE INPUT
LOW VOLTAGE INPUT
GND
Vref OUTPUT
Vcontrol INPUT

2 kΩ
MONITOR
POTENTIOMETER (*1) (10 kΩ)

*1: When using a potentiometer to adjust sensitivity, monitor the control voltage so it does not exceed +1.0 V.

TPMOC0154EC

Dimensional Outlines (Unit: mm)

□22.0 ± 0.5
14.0 ± 0.2
60.0 ± 0.5
450 ± 20
1.5 ± 0.2
("-06" Type: 0 ± 0.2)

φ10
WINDOW

EFFECTIVE AREA φ8
4-M2 DEPTH: 4

FRONT VIEW SIDE VIEW

Vcc Low Voltage Input : AWG26 (Red, +15 V)
Vee Low Voltage Input : AWG26 (Green, -15 V)
GND : AWG26 (Black)
Vref Output : AWG26 (Blue, +1.2 V)
Vcontrol Input : AWG26 (White, +0.25 V to +0.9 V)
Signal output : RG-174/U

TPMOA0012EC
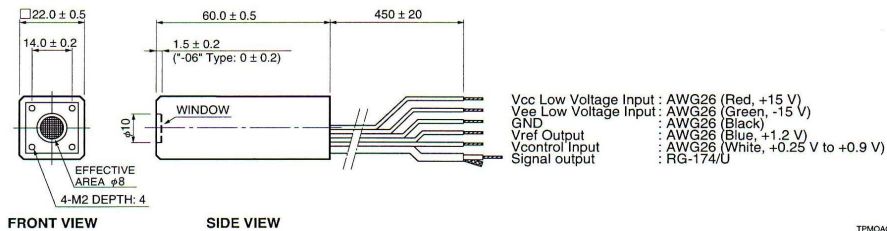
Option (Optical Fiber Adapter) (Unit: mm)

E5776 (FC Type)

□22.0 ± 0.5
14.0 ± 0.2
8.5 3.5 ± 0.2

4-M2 FC-R
FRONT VIEW SIDE VIEW TACCA0055EA

E5776-51 (SMA Type)

□22.0 ± 0.5
14.0 ± 0.2
10.7 5.0

4-M2 SMA 3.0
FRONT VIEW SIDE VIEW TACCA0239EA

Figure A.7 Specification sheet of PMT contd.

REFERENCES
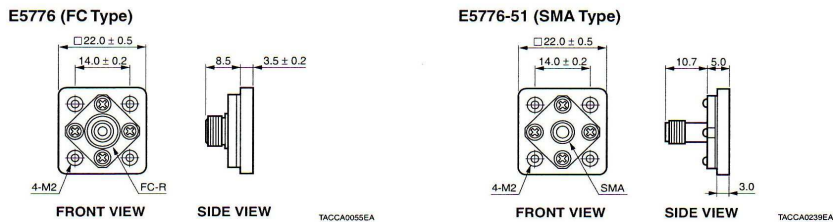
[1] P. T. C. So, T. French, W. M. Yu, K. M. Bernard, C. Y. Dong, and E. Gratton, "Time-resolved fluorescence microscopy using two-photon excitation," *Bioimaging*, vol. 3, p. 49, 1995.

[2] P. T. C. So, H. Kim, and I. E. Kochevar, "Two-photon deep tissue ex-vivo imaging of mouse dermal and subcutaneous structures," *Optical Society of America*, vol. 3, p. 339, 1998.

[3] W. Denk, J. H. Strickler, and W. W. Webb, "Two-Photon Laser Scanning Fluorescence Microscopy," *Science*, vol. 248, p. 73, 1990.

[4] R. M. Williams, W. R. Zipfel, and W. W. Webb, "Multiphoton microscopy in biological research," *Current opinion in chemical biology*, vol. 5, p. 603, 2001.

[5] R. Yuste and W. Denk, "Dendritic spines as basic functional units of neuronal integration," *Nature*, vol. 375, p. 682, 1995.

[6] J. Noguchi, M. Matsuzaki, G. C. R. Ellis-Davies, and H. Kasai, "Spine-neck geometry determines nmda receptor-dependent Ca2+ signaling in dendrites," *Neuron*, vol. 46, p. 609, 2005.

[7] R. H. Christie, B. J. Bacskai, W. R. Zipfelv, R. M. Williams, S. T. Kajdasz, W. W. Webb, and B. T. Hyman, "Growth arrest of individual senile plaques in a model of alzheimers disease observed by in-vivo multiphoton microscopy," *J. Neurosci.*, vol. 21, p. 858, 2001.

[8] B. J. Bacskai, S. T. Kajdasz, R. H. Christie, C. Carter, D. Games, P. Seubert, D. Schenk, and B. T. Hyman, "Imaging of amyloid-beta deposits in brains of living mice permits direct observation of clearance of plaques with immunotherapy," *Nat. Med.*, vol. 7, p. 369, 2001.

[9] W. A. Mohler, J. S. Simske, E. M. Williams-Masson, J. D. Hardin, and D. J. G. White, "White, Dynamics and ultrastructure of developmental cell fusions in the Caenorhabditis elegans hypodermis," *Curr. Biol.*, vol. 8, p. 1087, 1998.

[10] J. M. Squirrell, D. L. Wokosin, J. G. White, and B. D. Bavister, "Long-term two-photon fluorescence imaging of mammalian embryos without compromising viability," *Nat. Biotechnol.*, vol. 17, p. 763, 1999.

[11] K. T. Jones, C. Soeller, and M. B. Cannell, "The passage of Ca2+and fluorescent markers between the sperm and egg after fusion in the mouse," *Development*, vol. 125, p. 4627, 1998.

[12] B. R. Masters, P. T. So, and E. Gratton, "Multiphoton excitation fluorescence microscopy and spectroscopy of in vivo human skin," *Biophysical Journal*, vol. 72, p. 2405, 1997.

[13] K. M. Hanson, M. J. Behne, N. P. Barry, T. M. Mauro, E. Gratton, and R. M. Clegg, "Two-photon fluorescence lifetime imaging of the skin stratum corneum pH gradient," *Biophysical Journal*, vol. 83, p. 1682, 2002.

[14] T. P. Thomas, M. T. Myaing, J. Y. Ye, K. Candido, A. Kotlyar, J. Beals, P. Cao, B. Keszler, A. K. Patri, T. B. Norris, , and J. R. B. Jr., "Detection and Analysis of Tumor Fluorescence Using a Two-Photon Optical Fiber Probe," *Biophysical Journal*, vol. 86, p. 3959, 2004.

[15] N. A. Papadogiannis, B. Witzel, C. Kalpouzos, and D. Charalambidis, "Observation of Attosecond Light Localization in Higher order Harmonic Generation," *Physical Review Letters*, vol. 83, p. 4289, 1999.

[16] M. Wolf, E. Knoesel, and T. Hertel, "Ultrafast dynamics of electrons in image-potential states on clean and Xe-covered Cu(111)," *Phys. Rev. B*, vol. 54, p. R5295, 1996.

[17] M. Dantus, M. J. Rosker, and A. H. Zewail, "Real time femtosecond probing of transition states in chemical reactions," *J. Chem. Phys*, vol. 87, p. 2395, 1987.

[18] A. H. Zewail, "Laser femtochemistry," *Science*, vol. 242, p. 1645, 1988.

[19] R. D. Roorda, T. M. Hohl, and G. M. R. Toledo-Crow, "Video-rate nonlinear microscopy of neuronal membrane dynamics with genetically encoded probes," *J. Neurophysiology*, vol. 92, p. 609, 2004.

[20] Y. Barad, H. Eisenberg, M. Horowitz, and Y.Silberberg, "Nonlinear scanning laser microscopy by third harmonic generation," *Appl. Phys. Lett.*, vol. 70, p. 922, 1997.

[21] C. Rulliere, *Femtosecond Laser Pulses - Principles and Experiments (2nd Ed.).* Berlin, Germany: Springer, 2005.

[22] Ultrafast Laser Beamsplitter. [Online]. Available: https://www.newport.com

[23] J. K. Ranka, A. L. Gaeta, A. Baltuska, M. S. Pshenichnikov, and D. A. Wiersma, "Autocorrelation measurement of 6-fs pulses based on the two-photon-induced photocurrent in a gaasp photodiode," *Optics Letters*, vol. 22, p. 1344, 1997.

[24] Hollow Retroreflectors. [Online]. Available: https://www.edmundoptics.com

[25] NI labVIEW. [Online]. Available: https://www.ni.com/labview

[26] A. E. Siegman, *Lasers.* CA, USA: University Science Books, 1986.

[27] Photonic crystal fibers. [Online]. Available: https://www.crystal-fibers.com

[28] P. N. Prasad, *Introduction to Biophotonics.* NJ, USA: Wiley-Interscience, 2003.

[29] T. Vo-Dinh, *Biomedical Photonics Handbook.* NY, USA: CRC Press, 2003.

[30] A. Diaspro, *Confocal and Two-Photon Microscopy - Foundations, Applications and Advances.* NY, USA: Wiley-Liss, 2002.

[31] H. Schneckenburger, R. Steiner, W. Strauss, K. Stock, and R. Sailer, *Fluorescence technologies in biomedical diagnostics, Optical Biomedical Diagnostics.* Bellingham, WA: SPIE Press, 2002.

[32] P. R. Callis, "Two-photon-induced fluorescence," *Annu. Rev. Phys. Chem.*, vol. 48, p. 271, 1997.

[33] G.-M. Maria, "Uber Elementarakte mit zwei Quantensprungen," *Ann. Phys. Leipzig*, vol. 5, p. 273, 1931.

[34] W. Kaiser and C. B. G. Garret, "Two-photon excitation in calcium flouride molecule," *Physical Review Letters*, vol. 7, p. 229, 1961.

[35] S. Singh and L. T. Bradley, "Three-photon absorption in naphthalene crystals by laser excitation," *Physical Review Letters*, vol. 12, p. 612, 1964.

[36] A. Diaspro, *Building a two-photon microscope using a laser scanning confocal architecture-Methods of cellular imaging.* NY, USA: Oxford University, 2001.

[37] W. H. Louisell, *Quantum Statistical Properties of Radiation.* NY, USA: Wiley, 1978.

[38] D. L. Andrews, "Simple statistical treatement of multiphoton absorption," *Am. J. Phys*, vol. 53, p. 1001, 1985.

[39] F. A. Moscatelli, "Simple conceptual model of two photon absorption," *Am. J. Phys*, vol. 54, p. 52, 1986.

[40] P. T. C. So, K. H. Kim, C. Buelher, B. R. Masters, L. Hsu, and C. Y. Dong, *Basic principles of multi-photon excitation microscopy - Methods in Cellular Imaging.* NY, USA: Oxford University, 2001.

[41] Semrock. [Online]. Available: https://www.semrock.com

BIOGRAPHICAL STATEMENT

Priyanka Amrita Jillella was born in Narsapur, in the state Andhra Pradesh, India, to Percy and Amruta Kumar Jillella. She grew up traveling all over India and saw many places. She did her schooling in Kendriya Vidyalaya Sanghatan schools all over India. After graduating from high school, she pursued her B.Engg. in Biomedical Engineering from Mahatma Gandhi Mission's College of Engineering and Technology, Navi Mumbai, India. In her final year of her undergraduate studies she did her internship in BPL Ltd, Health Care Division, Mumbai, India.

After completion of her bachelor of engineering she joined Apollo hospitals as a trainee engineering where she learnt about various imaging and patient monitoring equipments. To learn and contribute towards medical imaging had always been her goal and for this reason she wanted to study further.

She joined University of Texas at Arlington to pursue MS in Biomedical Engineering. She worked on various course projects that taught and honed her programming skills. In her first semester in UTA she was introduced to the field of optics and its biomedical applications and she joined optical imaging lab the following semester. The projects she worked on involved, optical designs and setup, optoelectronic designs, interfacing hardware to software and mathematical simulations of optical medium. She successfully designed and developed a femtosecond pulse diagnosis and pulse delivery setup, she studied femtosecond pulse propagation in dispersive media and built an experimental multiphoton microscopy system.